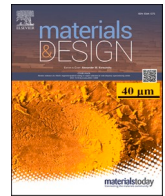| Title | Comparison of in-plane compression of additively manufactured Ti6Al4V 2D auxetic structures: Lattice design, manufacturing speed, and failure mode |
|---|---|
| Author(s) | Eren, Zana; Gokcekaya, Ozkan; Balkan, Demet et al. |
| Citation | Materials and Design. 2024, 241, p. 112885 |
| Version Type | VoR |
| URL | https://hdl.handle.net/11094/97263 |
| rights | This article is licensed under a Creative Commons Attribution 4.0 International License. |
| Note | |

# Comparison of in-plane compression of additively manufactured Ti6Al4V 2D auxetic structures: Lattice design, manufacturing speed, and failure mode

Zana Eren [a,*], Ozkan Gokcekaya [b,c,*], Demet Balkan [a], Takayoshi Nakano [b,c], Zahit Mecitoğlu [a]

[a] Faculty of Aeronautics and Astronautics, Istanbul Technical University, Istanbul, 34367, Turkey
[b] Division of Materials and Manufacturing Science, Graduate School of Engineering, Osaka University, 2-1, Yamadaoka, Suita, Osaka 565-0871, Japan
[c] Anisotropic Design & Additive Manufacturing Research Center, Osaka University, 2-1, Yamadaoka, Suita, Osaka 565-0871, Japan

## ABSTRACT

The metal-based 2D auxetic lattice structures hold the potential for multifunctional tasks in aerospace applications. However, the compression response of those manufactured by powder bed fusion process is underexplored. This study proposes a comprehensive comparison of in-plane quasi-static compression performance of 2D auxetic lattice structures, utilizing three designs (anti-tetrachiral (ATC), double arrow-headed (DAH), and tree-like re-entrant (TLR)), manufactured with stiff Ti6Al4V by the electron beam powder bed fusion process (PBF-EB) with various manufacturing speeds. The results revealed unique failure patterns and superior energy absorptions among 2D lattice structures in the literature. TLR design enhanced energy absorption by overcoming failures between DAH columns and exhibited the lowest standard deviations in specific energy absorption (SEA) values (9.75 %–12.62 %). Besides, Kernel average misorientation (KAM) values followed the order of DAH, TLR, and ATC, and inversely correlated with SEA values. ATC structures with the lowest KAM outperformed DAH and TLR by 47.5 % and 6.44 %, respectively. Scan speed variations affected SEA and porosity values differently for each lattice design while exhibiting similar microstructure characteristics. The findings in this study propose a significant contribution to the development of aerospace sandwich structures where harsh environments exist and employment of 2D topologies are required.

## 1. Introduction

Mechanical metamaterials are artificially created cellular materials that exhibit negative index properties, which are rarely found in nature. Within the scientific literature, there has been significant interest in lattice structure-based metamaterials with a negative Poisson's ratio, often referred to as auxetic structures, due to their unconventional behavior under different loading conditions [1,2]. In a broader aspect, auxetic structures have been found to enhance the performance of structures in various applications, such as sound absorption [3–6], vibration damping [7–9], morphing [10–14], and impact mitigation [15–25], particularly in the aerospace and defense industries [26]. Fig. 1-a illustrates a conventional topology which is a honeycomb lattice structure and three auxetic topologies which are re-entrant, anti-tetrachiral (ATC), and double arrow headed (DAH). When the topologies in x-y plane are extruded in 3rd dimension, they are named as the 2D lattice structures. 2D auxetic lattice structures exhibiting negative Poisson's ratio in in-plane directions (x-y plane) are of interest (Fig. 1-b) because of their high load bearing and impact mitigation performance under in-plane loading (x, y directions). Additionally, they fit in the specific geometrical limits for certain multifunctional tasks such as sound absorption, or directing cooling fluid flow inside the cells [27]. Notably, the chiral and re-entrant families are well-known examples of auxetic structures. Ma et al. [28] have shown that 2D ATC lattice structures from the chiral family outperform hexagonal honeycomb lattice structures in sound absorption. Ranjbar et al. [29] showed that ATC lattice structures exhibit enhanced performance for vibration damping when used in sandwich applications. Furthermore, Li and Yang [30] demonstrated that 2D DAH lattice structures, a member of the re-entrant family, exhibit higher vibration damping and bending stiffness than hexagonal

---

honeycombs. Regarding impact energy absorption, conventional honeycomb structures are broadly used in their out-of-plane direction (Fig. 1-**b**) in sandwich structures. However, when utilized in the in-plane direction, they exhibit a low load-bearing capacity. Yang et al. [17] presented that sandwiches with the core of auxetic re-entrant lattices exhibited enhanced ballistic resistance compared to sandwiches with conventional aluminum foam core. Hou et al. [21] experimentally demonstrated that sandwiches with auxetic re-entrant core outperformed sandwiches with conventional core designs (in-plane placement of truss, hexagon). Bohara et al. [31] presented a review study for the auxetic structures under blast-type shock loads where examples of auxetic structures showed enhanced energy dissipation performances compared to conventional core designs in sandwiches. To harness the different mechanical properties of 2D auxetic structures, their compression response in the in-plane direction is of interest such as ATC from chiral family, and DAH from re-entrant family. For instance, Günaydın et al. [32,33] found that a certain design of 2D ATC lattice structures made of Acrylonitrile Butadiene Styrene (ABS) polymer can absorb more energy than 2D re-entrant auxetic structures under compression loading. When in-plane loading (impact or compression) is applied to the struts, stiff circular hollow edges provide a strong bending resistance for the struts. Günaydın et al. [33] demonstrated that this type of unit cell behavior also played a role in having a higher energy absorption than re-entrant lattice structures. Li et al. [34], demonstrated that polymeric re-entrant lattice structures with reinforced two-phase cores can absorb twice as much energy as chiral and hexagonal honeycomb biphasic lattice structures under the in-plane low-velocity impact. Recently, Zhou et al. [35] demonstrated that 2D DAH lattice structures, made of nylon or Onyx material, exhibit superior SEA performance compared to hexagon and re-entrant lattice structures. Manipulating unit cell angles can also enhance the performance of auxetic structures. For instance, Chen et al. [36] numerically enhanced the blast mitigation performance of DAH lattice sandwiches by employing larger inclination angles in unit cells. The unit cell dimensions of DAH lattice structures can be adjusted to have higher compressive strength or stiffness based on the in-plane elasticity equations in the study, conducted by Qiao and Chen [37]. Li et al. [38] showed that origami structures outperform 2D re-entrant lattice structures in energy absorption with relatively more uniform mechanical properties in all directions during their compression with 304 steel and laser powder bed fusion (PBF-L) process. For 2D auxetic lattice structures, several studies have specifically investigated change of negative Poisson's ratio and elasticity modulus based on the

variation of the unit-cell parameters, including chiral, anti-tri-chiral, and anti-tetrachiral lattices [39], DAH lattices [37] and their U-type variations [40], as well as 2D tree-like re-entrant (TLR) lattices [41]. There are also recent studies reporting novel topologies with enhanced auxeticity and stiffness manufactured using PLA and FFF 3D printing [42,43], hybrid topology based 3D lattice structures manufactured using interlocking method and carbon fiber reinforced polymer [44,45]. Gao et al. [41] presented the theoretical relation between elasticity modulus and Poisson's ratio for TLR lattices. As DAH lattices gain recent interest as given above for impact mitigation and blast loading cases, its stiffer version TLR lattices which were reinforced with vertical struts require plastic deformation investigations under various loading regimes and different material stock. However, the comparison of deformation and energy absorption of auxetic structures such as those containing 2D DAH, ATC, and TRL lattices, or those manufactured with various non-polymeric materials, remains unexplored.

Particular attention is directed toward metallic cellular materials, specifically the Ti6Al4V alloy, which finds extensive use in the aerospace industry due to its high strength, lightweight properties, and availability for working in high temperatures. PBF techniques for metals, such as PBF-EB and PBF-L process, have enabled the fabrication of cellular structures from various types of metal alloys with a high dimensional accuracy [46]. Ding et al. [47] specifically investigated how dimensional accuracy can be increased when strut thickness and inclination angle in powder bed vary. Other additive manufacturing techniques rather than powder bed based techniques can also be employed to fabricate metal-based parts [48,49]. However, when compared to parts fabricated using these techniques, PBF parts enable the creation of metal microstructures with strength comparable to conventional counterparts [50]. Additionally, multi-material parts can be obtained as dissimilar powders are melted through a graded transition in the PBF processes [51]. The PBF-EB results in reduced residual stresses within the manufactured parts and minimizes the likelihood of oxidation occurring due to its processing conditions [52]. Furthermore, outcomes from the PBF-EB technique often eliminate the need for post-processing steps to alleviate stress within the components, which is useful for faster production cycles within the industry. On the other hand, Vaysette et al. [53] showed that the parts produced using PBF-L exhibit better surface roughness than PBF-EB parts resulting in better high-cycle fatigue performance. Koutiri et al. [54] demonstrated that variations in build angle, hatch distance, and volumetric laser energy density in PBF-L process enable obtaining better surface roughness. PBF-
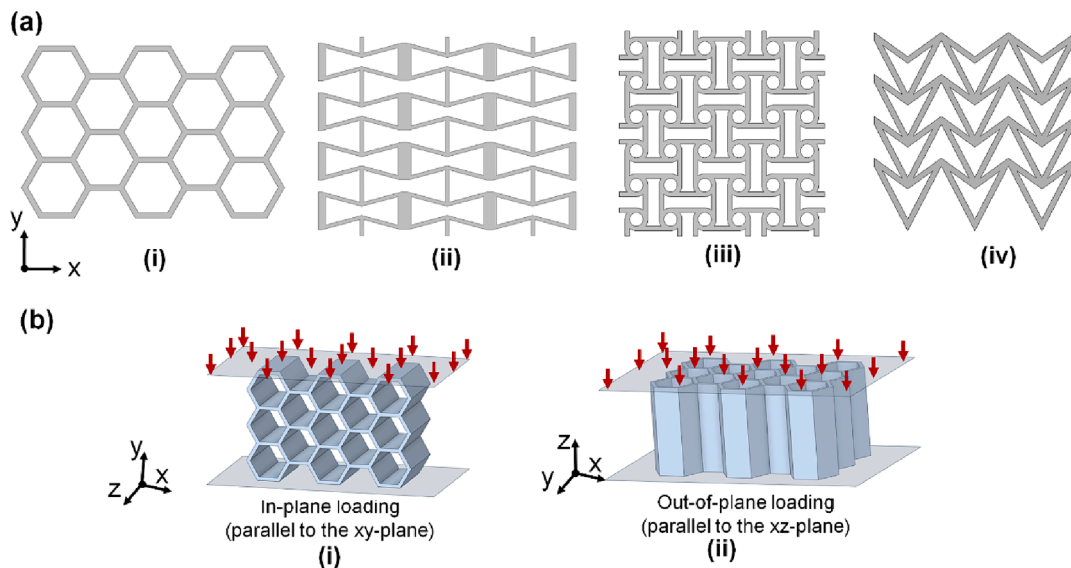


**Fig. 1.** (a) Example topologies of conventional and auxetic type 2D lattice structures. (i) Hexagonal honeycomb. (ii) Re-entrant (thickened inter-columns). (iii) Anti-tetrachiral. (iv) Double arrow headed. (b) Visual representation of "in-plane" type and "out-of-plane" type loading on a 2D lattice structure.

L with a thermal post process can be an option to enhance mechanical properties for particularly limited shape distortions [55]. Nevertheless, powder bed fusion-related defects, such as micro porosities, surface roughness, and inherent anisotropy, can significantly influence the crushing behavior and failure modes of cellular parts. Cansizoglu et al. [56] found that Ti6Al4V lattice structures, manufactured using the PBF-EB process in different build orientations, exhibit significantly varying compressive strengths. Xiao et al. [57] demonstrated that geometrical and surface irregularities on Ti6Al4V rhombic dodecahedron lattice structures lead to an apparent reduction in strength, with a size effect observed for specimens under 4 mm in size. Du Plesis et al. [58] found that increasing porosities in Ti6Al4V gyroid lattice structures, manufactured using PBF-L process, decreased the strength of the lattice structures, and this effect was more detrimental than lack of fusion defects. Ataee et al. [59] observed both brittle and ductile compressive formations for Ti6Al4V gyroid scaffolds. Cutolo et al. [60] obtained different shear bands in compressions of Ti6Al4V diamond-based lattice structures manufactured at different orientations in the powder bed. Li et al. [61] observed the failure modes of Ti6Al4V FCCZ and BCCZ lattice structures under compressive load. While BCCZ lattice structures exhibited failures in the form of buckling, FCCZ lattice structures exhibited abrupt shear failures. Choy et al. [62], observed different compression failure modes for Ti6Al4V 3D cubic and honeycomb lattice structures (of different lattice diameters) with increasing relative densities (i.e., layer by layer, diagonal shear band, V-shaped compression/band). Designs with low relative density were compressed layer by layer, while those with higher relative density exhibited diagonal bands and crack-based formations. The diameters or number of perpendicular struts in loading directions were found to be decisive in the development of energy absorption or failure bands during compression. Del Guercio et al. [63], found that the absorbed compression energies of Ti6Al4V X-type PBF-EB-manufactured lattice structures were closely correlated with relative densities.

The motivation for this study is to gain insights into the compressive response of auxetic 2D lattice structures, by considering energy absorption enhancements due to the topology and the base material of lightweight aerospace alloys Ti6Al4V, to meet the demands of aerospace missions that require both lightweight and withstanding high temperatures. Reminding that previous studies report enhanced performance for polymeric 2D auxetic topologies such as ATC and DAH lattice structures in impact, compression, or sound absorption. Meanwhile, auxetic TLR lattice structures, representing a stiffened version of DAH lattice structures with vertical struts, have the potential to enhance specific energy absorption, especially with an increasing number of struts. However, there is currently no report for the compression response of these three 2D topologies when additively manufactured with Ti6Al4V alloy. Additionally, the Ti6Al4V alloy produced through the PBF-EB process can exhibit lower ductility than conventional counterparts due to defects occurring in the PBF processes. In this manner, the obtained failure behavior during compressions is expected to significantly differ from previously reported ones for polymers such as the polymeric ATC geometry [33], and polymeric DAH geometry [35]. Moreover, prior investigations into various lattice structures manufactured using the PBF process have highlighted the substantial impact of manufacturing-related outcomes, including micro-porosities, surface quality, and build orientation, on structural performance. In aerospace applications, especially those involving load-bearing and fluid flow channels, understanding how the structural response may vary in repetitive tests (variation of the standard deviation) is crucial. Another important consideration, particularly in industrial cases, is the potential impact of increased manufacturing speed, which has not been investigated thus far. When lattice structures are fabricated using the PBF-EB process, the speed of the process can affect the microstructures of the samples. Consequently, a critical question arises regarding how these speed-related factors influence the obtained performance of specifically selected topologies, particularly in terms of compressive energy absorption.

This study proposes and investigates a novel combination for the in-plane quasi-static compression of 2D auxetic lattice structures as shown in Fig. 2. This combination includes **(i)** employing 2D auxetic topologies (anti-tetrachiral, double arrow headed, and tree-like re-entrant lattice structures) with promising energy absorption capacities, **(ii)** utilizing aerospace grade material (Ti6Al4V material) using PBF-EB process, **(iii)** adjusting beam scan speed in the PBF-EB process within a suitable constant energy density window to measure effect on the compressive response. The results of repeated compressive tests were compared through reaction force–deformation curves and specific energy absorptions. Micro-characterization methods were employed to investigate whether microstructural properties, texture structure, micro porosities, and residual stresses were effective on the macro mechanical response at critical struts. Furthermore, experimental deformations were followed by finite element analyses, aiming to obtain similar deformation patterns and energy absorptions consistent with the experiments.

## 2. Materials and methods

### 2.1. Lattice structure designs

This sub-section summarizes selected geometries (Anti-tetrachiral (ATC), Double Arrow Headed (DAH), and Tree-like Re-entrant (TLR)) for designing, and manufacturing in PBF-EB process. To use auxetic lattice structures in load bearing, compression, or impact mitigation applications under various loading conditions, these should pose initially sufficient stiffness. ATC, DAH, and TLR lattice blocks were designed with a total width of 50 mm, consisting of 5 x 5 cells to compare each other. To facilitate the manufacturing process and observe plastic deformations with a reasonable compressive reaction force, a depth (extrusion direction of 2D topology/z direction in Fig. 3**(ii)**) of 25 mm was selected. Fig. 3-**a** shows the unit cell parameters of $L_x$, $L_y$, $r$ of ATC lattices which are the length of distance between two edge centers in x and y directions, the radius of edge circles, respectively. Unit cell of DAH lattices is illustrated in Fig. 3-**b**, and $\theta_1$ and $\theta_2$ represent angles at buckling points, influencing the relationship between $E_y$ and $\theta_1$, $\theta_2$. The dimensions of the lattice structures used for manufacturing are as follows: ATC block (50 mm x 50 mm x 25 mm), DAH block (50 mm x 45 mm x 25 mm), and TLR block (50.6 mm x 51.6 mm x 25 mm). The relative volumes (calculated by dividing the total material volume by the volume of the enclosing box) are determined as 0.498, 0.572, and 0.477. It is important to maintain the depth of the 2D lattice blocks (in the non-cellular material direction or z-direction, as shown in Fig. 3) at a reasonable level; otherwise, their relative volumes increase dramatically.

### 2.2. Lattice structure manufacturing

#### 2.2.1. Materials

A Ti6Al4V (Ti64) spherical powder was purchased from Arcam AB (Sweden), which was produced by plasma atomization and used as the starting material in this study. The Ti64 powder size distributions (PSD) were measured using a Mastersizer 3000E (Malvern Panalytical, UK), showing size distributions of D10, D50, and D90 were 60.3, 82.3, 110.9 μm, respectively (Fig. 4). The composition of Ti64 powders used in this study is given in Table 1. The commercial Ti64 powders were spherical with some satellites, exhibiting good flowability and packing density while avoiding smoke error which is a common problem due to poor powder quality [64].

#### 2.2.2. Electron beam powder bed fusion (EB-PBF)

ARCAM's PBF-EB system (Arcam Q10, ArcamAB, acquired by GE Additive) was utilized for the fabrication of the samples. To narrow down the process parameters, cubic samples measuring 1x1x1 cm$^3$ were printed with different parameters. After visually inspecting the cubes, a
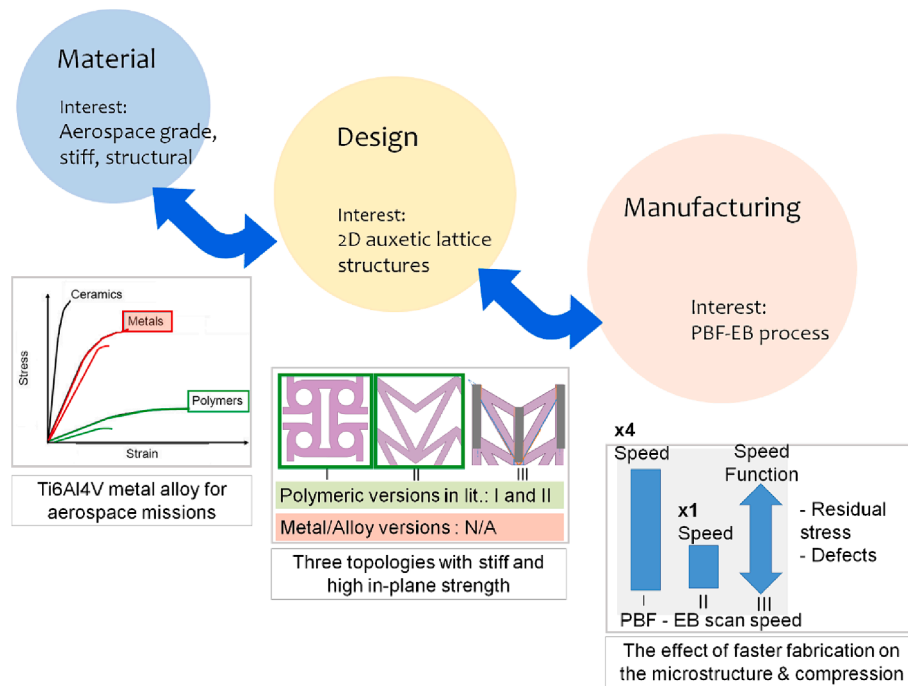
**Fig. 2.** Designated combination for the present in-plane compression study: (i) stiff Ti6Al4V material from PBF-EB process, (ii) 2D auxetic lattice topologies with promising in-plane energy absorptions, (iii) various manufacturing speeds at PBF-EB process to identify effects of microstructural variations when fabricated structures are compressed.

few selected parameter sets were used to print unit cells of three lattice types. The manufacturing of lattice blocks was then carried out using the three sets of parameters specified in Table 2. The automatic scan speed function (SF) refers to a black box function that was applied during the process by the machine's software to vary the scan speed. Two other sets of parameters, with low speed (LS) and high speed (HS) beam scans, were utilized to fabricate samples with an electron beam energy density constraint of 24 J/mm³. Within this constraint, the effects of different scan speeds and the performance of each lattice design were evaluated. 0° build orientation refers to the 2D topology of the lattices (x-y plane in Fig. 3) that were built parallel to the horizontal axis of the powder bed.

Fig. 3-d shows the front view of 2D lattice structures, which have 5 x 5 cells and were manufactured using the PBF-EB process with designed dimensions. The masses of designed ATC, DAH, and TLR lattice structures are 138.04 g, 142.60 g, and 138 g respectively. To ensure statistical significance, 5 samples were fabricated and compressed for each type, resulting in a total of 15 samples.

### 2.3. Microstructural characterization

In order to predict the relation of the failure mechanism and microstructural features, the microstructure characterizations were carried out focusing on the thin walls of each lattice design and scan speed.

#### 2.3.1. Defects and strut thickness evaluations

The as-built Ti64 lattices were investigated in terms of production-induced porosity and strut thickness. The production-induced defects on x-y cross-section and porosity measurements on y-z plane of the thin wall were carried out (Fig. 3) for each lattice design fabricated with different process parameters, besides, the strut thickness of each sample was investigated on x-y cross-section (vertical to build direction). The porosity and strut thickness assessments were performed on images obtained by optical microscopy and the application of the image analysis software ImageJ.

#### 2.3.2. Microstructure evaluations

Microstructure observations were carried out for the x-y plane (same axes in Fig. 3) of a single thin wall of different lattice designs fabricated by PBF-EB with different process parameters (SF, HS, and LS). The x-y cross-section of the thin wall of the lattices was obtained from the mid-section by electrical discharge wire cutting and mirror-polished. The single thin wall of the lattice structures was observed by filed-emission scanning electron microscopy (FE-SEM; JEOL JIB-4610F, Japan) equipped with an electron backscatter diffraction system (EBSD, Nor-dlysMax3 system, Oxford Instruments, UK) operated with a 20 kV accelerating voltage. The microstructural features, such as the grain size, pole figure, inverse pole figure (IPF) map, phase distribution map, and Kernel average misorientation (KAM) map, were assessed by HKL Channel 5 software (Oxford Instruments, Cambridge, UK).

### 2.4. Quasi-static compression testing

The MTS 600 kN capacity static-hydraulic universal test system (Criterion® Series 60, Model 64.605) was utilized in conducting compression tests on the lattice structures, with a constant compression rate of 5 mm/min. The lattice structure was placed between two platens of the test frame (Supp. Fig. S1), with the top plate held in a fixed position while the bottom plate compressed the lattice structure and experiments were repeated five times for each condition. For safety reasons, the tests were automatically terminated when the compression strain dropped by 95 %. The compression results were assessed in terms of specific compressive strength, absorbed energy (EA), specific energy absorption (SEA), and crushing load efficiency (CLE). EA is the area under the force–deformation curve of the compression. SEA is calculated when EA is divided by the mass of the compressed block. CLE is calculated in two ways; the first one is the ratio of mean crushing force (MCF) to peak crushing force (PCF), and the second one is calculated as dividing plateau stress at a certain point to peak compressive strength. The comparisons of the results were given in section 3.2.4.
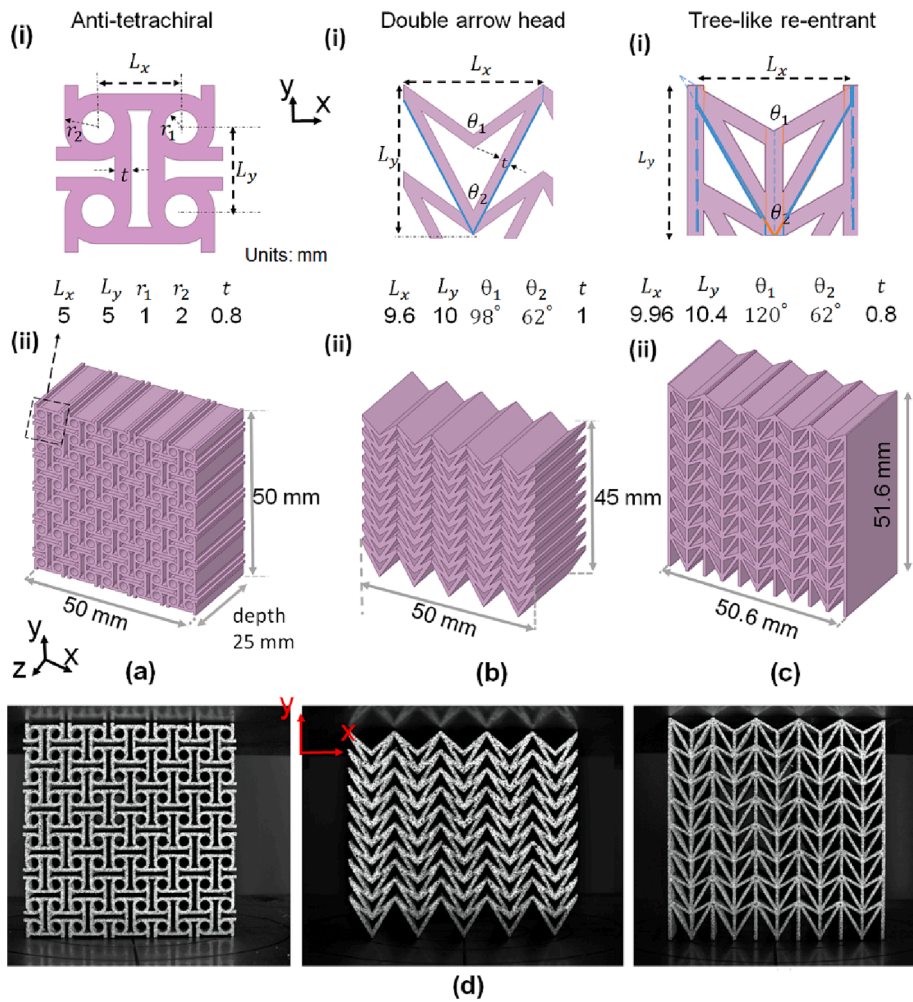
**Fig. 3.** (a) Anti-tetrachiral (ATC) (b) Double arrow headed (DAH) (c) Tree-like re-entrant (TLR) lattice designs with (i) unit cells parameters, (ii) blocks (2D auxetic lattice structures) (d) Manufactured lattice geometries of ATC, DAH, and TLR using PBF-EB process with Ti6Al4V material, respectively.
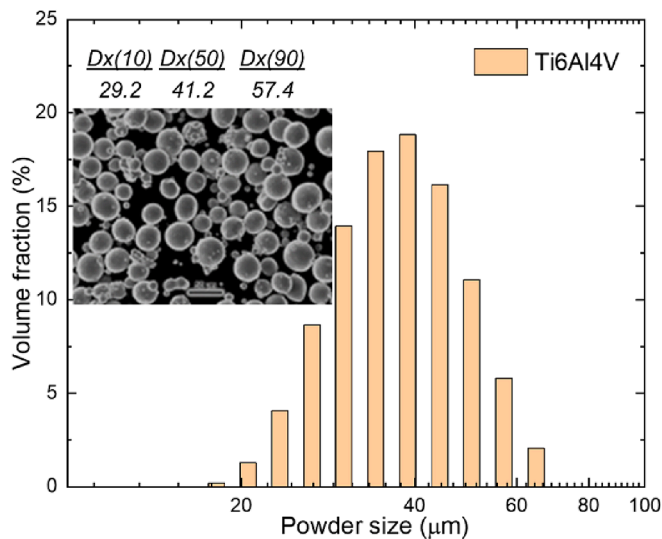


**Fig. 4.** Powder size distribution of Ti-6Al-4 V powders with a microscope image of the powders.

**Table 1**
Composition of the Ti6Al4V powder.

| Element | Al | V | C | O | Fe | N | H | Ti |
|---|---|---|---|---|---|---|---|---|
| **Weight (%)** | 6 | 4 | 0.03 | 0.15 | 0.1 | 0.01 | 0.003 | Balance |

### 2.5. Finite element analysis (FEA)

Finite element models were created in ABAQUS environment for the quasi-static compression. The model includes a lattice block, the fixed top platen, and the compressing bottom platen (**Supp. Fig. S2**). General contact algorithm was employed for contact interactions between i - compression platen and bottom portion of the structure, ii- top platen and top portion of the structure, iii - self contact of the structure (incorporating inner nodes-elements). For tangential contact behavior, 0.2 of static friction of coefficient was employed. For normal contact behavior, the hard type contact algorithm was utilized in terms of pressure over closure. The base material, Ti64, was modeled with a Young's modulus of 110 GPa, a density of 4430 kg/mm3, and a Poisson's ratio of 0.3 [65]. To simulate the post-elastic behavior, stress–strain tensile test data were utilized in Johnson-Cook (JC) strength and damage laws as studied in the previous work [66]. The JC parameters in Table 3 were employed in ABAQUS solver [67]. Relevant data for damage parameters in the literature [68–70] were taken into account for calibrations. The weak zones were utilized owing to outcomes from the experimental compression patterns which are later given in the results

**Table 2**

Employed PBF-EB process parameters to build lattice blocks at various beam scan speeds.

| Scan speed type | Built angle (°) | U (kV) | I (mA) | v (mm/s) | Line offset (mm) | Thickness (mm) | E (J/mm³) | Focus offset (mA) |
|---|---|---|---|---|---|---|---|---|
| High Speed (HS) | 0 | 60 | 20 | 10,000 | 0.1 | 0.05 | 24 | 10 |
| Low Speed (LS) | 0 | 60 | 5 | 2500 | 0.1 | 0.05 | 24 | 10 |
| Automatic Speed Function (SF) | 0 | 60 | SF(−160) | SF(−160) | 0.1 | 0.05 | – | 10 |

**Table 3**

Johnson-Cook plasticity and damage model parameters for Ti6Al4V, respectively.

| A (MPa) | B (MPa) | n | c** | m | Strain rate (1/s) | D1 | D2 | D3 | $G_C$ (MPa $\sqrt{m}$) |
|---|---|---|---|---|---|---|---|---|---|
| 870–950* | 450–550* | 0.34 | 0.029 | 0.8 | 1 | −0.05 | 0.27 | −0.48 | 49.9–100 |

\* The ranges for A and B aim to verify varied energy absorption for SF, HS, and LS lattice samples, however a single A, B set was used as only SF values were validated. **[68].

section (**Supp. Fig. S3**). C3D10M type elements with a unit length of 0.5 mm in the x-y plane and 1 mm in the extrusion direction were employed for meshing. A mesh convergence study was presented as a supplementary material (**Supp. Fig. S4**). As the explicit solver was employed [71], appropriate artificial mass scaling was utilized to accelerate analyses within the constraint of maximum 10 % kinetic energy of total internal energy.

## 3. Results and discussion

### 3.1. Microstructural characterization

The qualities of the samples were evaluated with respect to the microstructural features of lattice single walls to correlate with the fracture mechanism of lattice designs, as shown in Fig. 5 and quantitatively summarized in Table 4.

### 3.1.1. Defects and strut thickness evaluations

The structural integrity of each design was achieved although porosity was identified on x-y plane and y-z plane, as represented in Fig. 5 for the HS condition (**Supp. Fig. S5 and S6** for SF and LS conditions, respectively). The distribution of porosity in x-y and y-z planes of samples for each design and scan speed showed irregularity. ATC lattice exhibited similar porosity (Ave: 0.07 %) independently from the change

**Table 4**

Porosity, grain size, and KAM value of each unit cell with the change of lattice design and scan speed.

| Unit cell samples | Porosity (y-z plane, %) | Grain size (µm) | KAM (°) |
|---|---|---|---|
| **ATC** | SF: 0.08 | SF: 1.51 | SF: 0.71 |
| | HS: 0.07 | HS: 1.40 | HS: 0.66 |
| | LS: 0.08 | LS: 1.41 | LS: 0.65 |
| **DAH** | SF: 0.18 | SF: 1.40 | SF: 0.97 |
| | HS: 0.17 | HS: 1.37 | HS: 0.98 |
| | LS: 0.12 | LS: 1.34 | LS: 1.00 |
| **TLR** | SF: 0.08 | SF: 1.33 | SF: 0.83 |
| | HS: 0.02 | HS: 1.25 | HS: 0.91 |
| | LS: 0.18 | LS: 1.35 | LS: 0.82 |

in scan speed (Table 4). However, significant fluctuation in porosity was detected for DAH and TRL lattice designs with the change in scan speed. Thus, it is expected to observe inconsistency in compression test results and failure mechanisms. The strut thickness measurements from selected unit cells of lattice structures demonstrate that the lattice structures have thicknesses of 0.867 mm, 1.089 mm, and 0.859 mm, respectively, which are thicker than designed ones, 0.8 mm, 1 mm, and 0.8 mm (**Supp. Fig. S7**). It is noteworthy to mention that while focus offset and scan speed can alter the geometry of a scan track because of differences in cooling rates and eventual thermal history, the higher wall
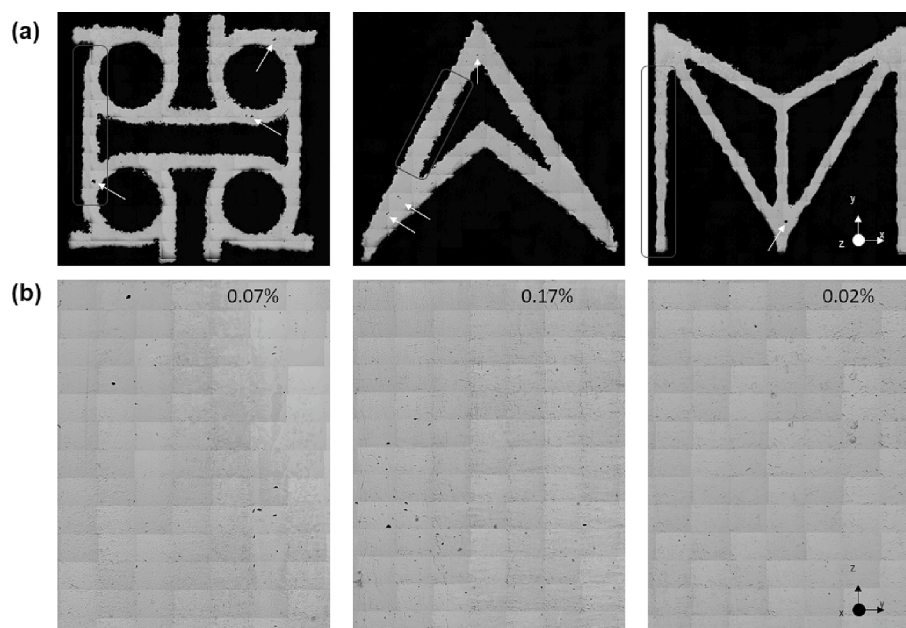


**Fig. 5.** Optical microscope images of ATC, DAH, and TLR lattices fabricated with high speed (HS) scanning condition by PBF-EB were observed on (a) x-y plane and (b) y-z plane to investigate porosity ratio, respectively (white arrows indicate porosities in x-y plane, red boxes indicate investigated strut for micro-characterization in y-z plane).

thickness of each lattice design was expected owing to attached powders during solidification, thus the difference in wall thickness can be related to this phenomenon.

### 3.1.2. Microstructural features regarding lattice design and scan speed

The difference in thermal history due to scan speed and/ or lattice design can vary the microstructure features (Fig. 6) owing to the beam exposure time and heat accumulation regarding strut relative density, respectively. Therefore, grain size and kernel average misorientation (KAM; demonstrate the remaining stress) varied with lattice design and process parameters (Table 4). Considering the effect of the process parameters, the contour scan strategy included in the standard SF processing condition deduced a bigger grain size for each lattice design, indicating enhanced heat accumulation by limiting thermal dissipation, thus proposed beneficial for mitigating residual stress [72]. However, the differences in grain size of lattice structures were not considered to be significant to affect the performance of the structures. On the other hand, the KAM value of lattices representing accumulated residual stress, which affects the level of absorbed energy, exhibited an ascending order as ATC < TRL < DAH (Table 4). This tendency was inversely related to the energy-absorbing performance of lattice structures, as discussed in the following sections (section 3.2.4.4). The variation in process parameters and changes in lattice design had no significant effect on phase formation. As shown in Fig. 6 (Phase map), a major α phase and minor β phase existed in the lattice structures. The phase formation of Ti64 processed by PBF-EB has been reported to follow the steps of (i) L → β, (ii) β → α', (iii) α'→α + β [73], corresponding to the findings of this study. While the α phase normally precipitates in β matrix, α grain precipitation follows the Burgers orientation relationship (BOR): (0001)α//(1 1 0)β, [11–20]α//[1 1 1]β. Within the BOR, there are 12 variations for α grains to form. The α variation selection can enhance mechanical properties in an anisotropic manner [74]. However, as identified by the pole figures in Fig. 6, the α grains followed BOR with no variant selection. Thus, an anisotropic property for lattice structures was not expected regarding the microstructure features.

### 3.2. Evaluation of compression performance

In this section, snapshots of the collapse modes of the lattice structures were given at different moments during the compression tests with 5 mm/min. As the structures were built in 0° orientation with three different scan speeds, three different compression histories were represented as rows in each figure (Figs. 7, 9, and 10). The sub-figures in columns show the beginning stage, early strut failures, and larger failure mode shapes that were initially developed, respectively. Next, developing mode shapes and separations are represented in the last columns, respectively. The compression deformations were supported with compression force–deflection curves including all test repetitions (Fig. 8).

### 3.2.1. Anti-tetrachiral (ATC) lattice structure

Fig. 7 summarizes the compression deformation of anti-tetrachiral lattice structures built in the 0° orientation with different scan speeds, with corresponding images for each type. General compression trends were observed across the five repetitions of tests, which included certain modes. However, establishing a distinct relationship between the collapse formations and different beam scan speeds was challenging, as many micro-defects could influence deformation modes. (SF, HS, and LS). Therefore, compression snapshots of a single sample for each type were given to provide representability. In summary, the compression trend for ATC lattice structures was as follows: local buckling was constrained as horizontal struts touched each other, and then local failures appeared. Initial local buckling and fractures were visible at compressions of 5–6 mm, highlighted with red dots in the second column of images in Fig. 7. The third column of images represented the main

collapse modes of the lattice structures, exhibiting similar modes of shear band formation from one top edge to the other cross lower edge of the block or V-shape band formation. This formation includes localized failures at struts and creates failure lines as described. It explicitly differs from the bending type collapse of anti-tetrachiral lattice structures produced with ABS polymer [33]. Additionally, its polymer version did not exhibit separation of un-crushed pieces from the test area. The fourth column of images represented the moment when some pieces started to separate from the samples. These results showed that compressions after 15 mm differed from each other mainly due to the local compression formations or local separations caused by failures. Notably, at this stage, force peaks and absorbed energies started to differ as there were separated non-crushed pieces in several tests, as highlighted in the next subsection. In the later stages of the compression, where broken lattices remained under the platen, the curve exhibited a higher response due to the compression of more lattice pieces. This phenomenon occurred because some pieces of the samples would break and separate, even if the separated cellular piece flew away without being crushed.

Fig. 8-a shows the reaction forces-deformation curves of ATC lattice structures. The SF, LS and HS groups exhibited peak reaction forces of $264.94 \pm 18.09$ kN, $276.14 \pm$ std $24.93$ kN, and $272.46 \pm$ std $8.18$ kN, respectively. Although the LS group exhibited coherent curve formations within itself, some of the curves progressed at higher rates. The average peak force of the LS group is the highest among all. At 10 mm, the SF, LS, and HS groups absorbed $1.27 \pm$ std $0.22$ kJ, $1.25 \pm$ std $0.21$ kJ, and $1.28 \pm$ std $0.04$ kJ, respectively. Additionally, while the trend followed an absorption range of around $1.2 – 1.3$ kJ, some cases reached values as high as $1.4 – 1.5$ kJ, possibly due to randomly progressed specific collapse shapes. At 15 mm, deviations in absorption levels become distinct, with values ranging between $1.48 – 2.38$ kJ. The SF, LS and HS groups absorbed energies of $1.89 \pm$ std $0.32$ kJ, $1.91 \pm$ std $0.32$ kJ and $1.93 \pm$ std $0.28$ kJ, respectively. At 20 mm, as expected, the standard deviation increased, because progressed fractures and failures affected deformation patterns, thereby influencing energy absorption. The SF and LS samples dissipated energies of $2.16 \pm$ std $0.38$ kJ and $2.33 \pm$ std $0.71$ kJ. Although three SF samples exhibited a standard deviation of 10 %, a deviation of 25 % was also recorded. While two LS samples absorbed energies between 1.88 and 1.96 kJ, one of the samples dissipated a significantly higher value of 2.86 kJ. The HS group dissipated energy of $2.22 \pm$ std $0.42$ kJ ranging from $1.75 – 2.25$ kJ, with one sample dissipating a significantly higher value of 2.85 kJ. Briefly, the LS samples absorbed the highest energy of all. The absorbed energy-deflection curves were given in Supp. Fig. S8.

### 3.2.2. Double arrow headed (DAH) lattice structure

Fig. 9 summarizes the compression deformation of DAH lattice structures built in the 0° orientation with different scan speeds, with images for each type. In summary, the compression trend was as follows: A short phase of elastic compression, exhibiting a negative Poisson's ratio, was followed by initiation of the local buckling at the bottom cells (deformed thin struts), as highlighted in the second column of Fig. 9. Then, initiated separations between cells, progressed between columns (or between cells), as shown in the third column. Additionally, a few lines of cells had already collapsed at that time. Next, a continuous line of failure separations between columns from bottom to top became apparent, as given in the fourth column. During the motion of the platen, some pieces of several samples separated without collapsing due to sudden fracture and did not contribute to the force–deformation responses. It is the critical outcome that if the connections between the columns were stronger, some of the columns would not lean towards the sides, and this would allow the structure to exhibit a longer period of elastic compression with a negative Poisson's ratio and local plastic buckling, which in turn could increase the energy absorption. The compression patterns with Ti64 material explicitly differ from the previous reports, which employed generic metal properties, due to earlier failures between cell columns. The response at higher velocities can
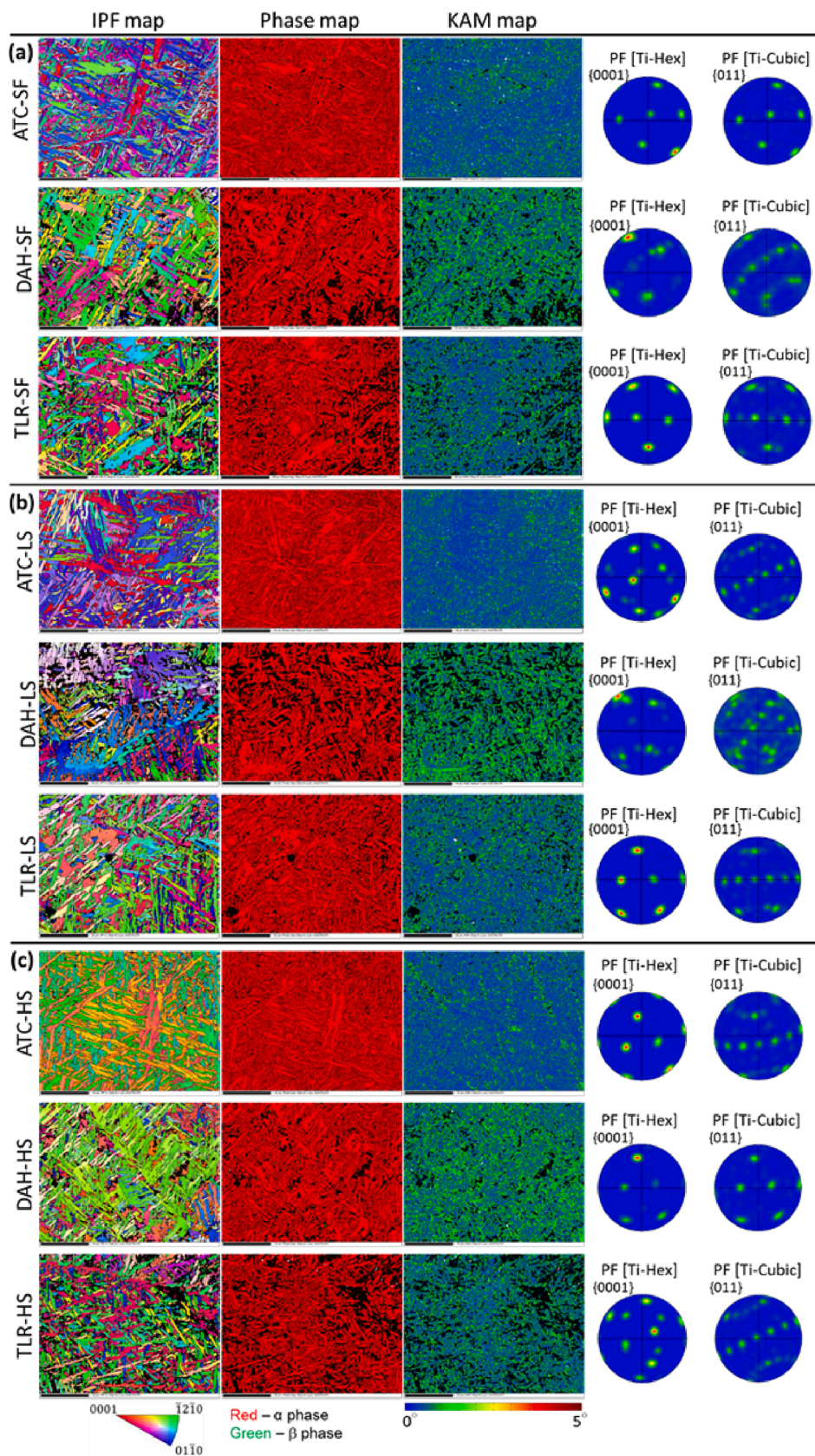
**Fig. 6.** SEM observations of a single thin wall on x-y plane for different lattice designs fabricated with varied scan parameters by EB-PBF, presenting inverse pole figure, phase distribution, and kernel average misorientation maps with corresponding α and β pole figures. The scale bar represents 20 μm. (For interpretation of the references to colour in this figure legend, the reader is referred to the web version of this article.)
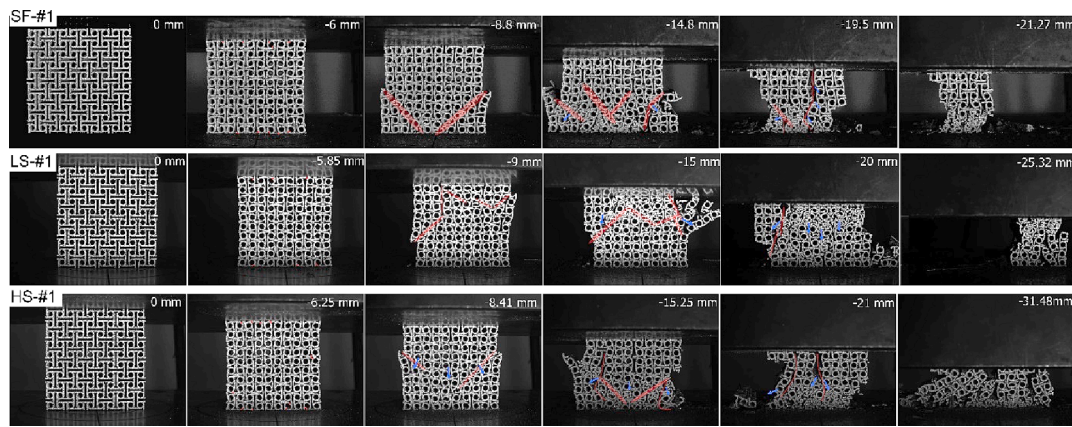
**Fig. 7.** Snapshots at certain times during compressions of ATC lattice structures: SF-#1, LS-#1, and HS-#1 samples, respectively (red lines represent failed connections/shear bands). (For interpretation of the references to colour in this figure legend, the reader is referred to the web version of this article.)

have fewer non-crushed pieces. However, stronger construction of the inter-columns can contribute to having higher energy absorption at various impact velocity regimes.

Fig. 8-b shows the reaction forces-deformation curves. The SF, HS, and LS groups exhibited peak reaction forces of 127.62 ± std 11.98 kN, 121.38 ± std12.65 kN, and 143.90 ± std 7.11 kN, respectively. At 10 mm, the SF, HS and LS groups dissipated energies of 0.74 ± std 0.08 kJ, 0.73 ± std 0.09 kJ, and 0.83 ± std 0.05 kJ, respectively. At 15 mm, deviations in absorption levels become distinct with values ranging between 1.75 − 2.5 kJ. The SF, HS and LS groups absorbed energies of 1.02 ± std 0.13 kJ, 1.00 ± std 0.18 kJ and 1.24 ± std 0.10 kJ, respectively. At 20 mm, as expected, the standard deviation increased because progressed fracture and failure affected deformation patterns, thus impacting the energy absorption. SFs absorbed energy of 1.23 ± std 0.19 kJ, ranging between 1.06 and 1.5 kJ. LS samples dissipated energy of 1.63 ± std 0.15 kJ, ranging between 1.471 and 1.777 kJ. The HS group dissipated energy of 1.27 ± std 0.27 kJ between 0.943 and 1.548 kJ (One sample did not crush until 20 mm). The LS group exhibited the highest absorption among all). (Supp. Fig. S7).

### 3.2.3. Tree-like re-entrant (TRL) lattice structure

Fig. 10 summarizes the compression deformation of TLR lattice structures built in the 0° orientation with different scan speeds, with images for each type. To follow the deformation of tree-like re-entrant lattice structures step by step, the motion can be summarized as follows: the vertical struts at the bottom row of the cells start to buckle, then some of them fail as shown in the second column. Local collapses progress at the bottom rows as shown in the third column. Unit cells continue to progressively collapse as shown in the fourth column. Until 19 mm compression, large pieces do not leave the samples. Then, 2–3 cells leave the sample without crushing, which might affect the energy absorption. As an advantage, the ratio of separated cells is still less than that of DAH ones. When compressions reach 25–30 mm, some large pieces leave the samples as shown in the last columns of images. According to Fig. 10, lattice structures built with different conditions exhibited clear and progressive collapse mechanisms. However, it was noted that in a few samples, the collapse started at the top section instead of starting at the bottom section due to the critical imperfections which possibly populated at the top section of the lattice blocks. General observation for the five repeats of each type of sample, of which the deformation patterns were coherent, despite employing three different scan speeds for manufacturing. The patterns also showed that vertical struts between columns contributed to solving the problem of DAH lattice structures which were early separations of some columns/cells without crushing. As there is no available report regarding the compression of the lattice structure with polymer base material, a comparison for the compression patterns cannot be made.

Fig. 8-c shows the reaction force-compression curves of tree-like re-entrant lattice blocks built at 0° with three different scan speeds. The SF, LS, and HS groups exhibited reactions of 200.32 ± std 12.02 kN, 214.27 ± std 9.80 kN, and 238.03 ± std 28.95 kN, respectively. It is understood that the HS group samples reached the highest peak forces among all tree-like lattice structures. At 10 mm, The SF, LS, and HS groups absorbed energies of 0.92 ± std 0.08 kJ, 0.83 ± std 0.05 kJ, and 0.73 ± std 0.09 kJ, respectively. Although peak forces could deviate due to vertical struts, subsequent formations of curves were decisive in determining the amount of absorbed energies. At 15 mm, The SF, LS, and HS groups absorbed energies of 1.50 ± std 0.13 kJ, 1.67 ± std 0.12 kJ, and 1.54 ± std 0.09 kJ, respectively. At 20 mm, The SF, LS, and HS groups absorbed energies of 1.98 ± std 0.25 kJ, 2.19 ± std 0.21 kJ, and 2.06 ± std 0.23 kJ, respectively. Namely, the LS group exhibited the highest absorption among all (Supp. Fig. S7).

Imperfections in vertical struts affected the initial peak forces, while subsequent peaks might have varied due to imperfections in vertical struts of the middle and top rows, leading to slight changes in the total absorbed energies. In previous lattice designs, under the same powder stock and process conditions, lattice blocks with tree-like re-entrant cells have been shown to exhibit higher energy absorption compared to DAH cells. This could be attributed to the fact that the manufactured tree-like re-entrant lattice structures exhibit a progressive collapse at each row of cells. While the vertical struts act as reinforcing elements between reverse arrow unit cells and enhance the ties between cells, they also increase peak reaction forces as they resist compression. However, other vertical struts passing through reverse arrows prevent the initiation of failures from those locations.

### 3.2.4. Comparative performance evaluation with microstructural results

#### 3.2.4.1. Peak reaction forces (PCF).
The peak reaction force represents the highest initial reaction force observed during impact or quasi-static compression tests on bulk or cellular structures. It is commonly used to calculate efficiency indicators for occupant safety components. Table 5 presents the average data along with standard deviations of the peak reaction forces, while Fig. 11-a illustrates the range of deviations observed in repeated tests for each sample. Additionally, micro-characterization data in Table 5 are employed to discuss their relationship.

(1) Notably, peak force results from five repeated tests for each sample type demonstrate that the anti-tetrachiral geometry exhibited 25 % higher average peak forces than those of the tree-like re-entrant ones.
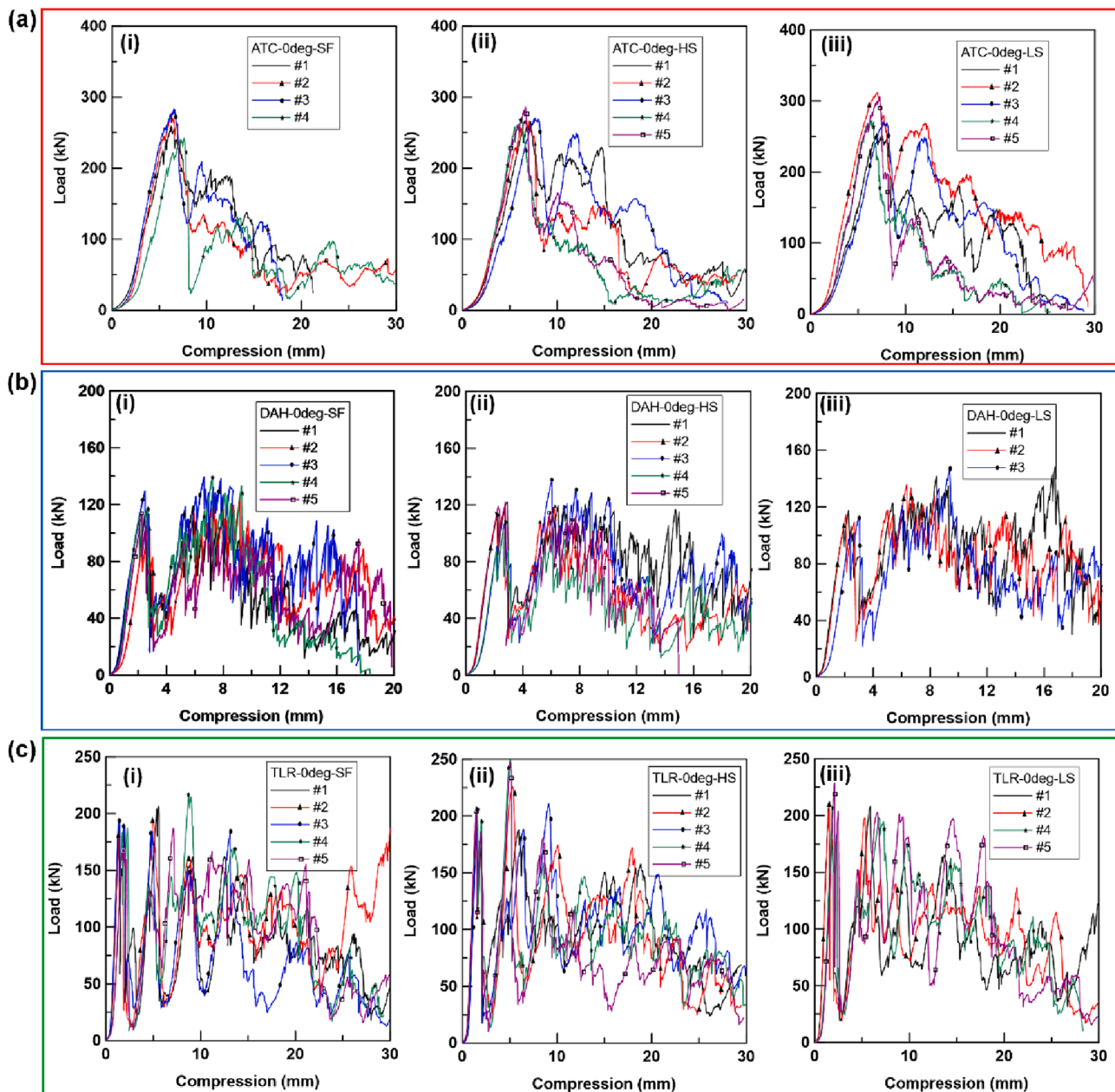
**Fig. 8.** Reaction load-compression curves of (a) ATC (b) DAH (c) TLR lattice blocks built by three different speed functions.

(2) As expected, the stiffer version of the DAH lattice structures, the tree-like re-entrant ones, exhibited higher peak reaction forces than the DAH ones (e.g., 49 % higher for LS type).

(3) However, for all types of geometries, there were significant standard deviations in the peaks of repeated tests, highlighting the influence of random imperfections obtained during manufacturing, which resulted in variations in the compressive initial strength of samples of the same type. This underscores the importance of conducting a greater number of tests compared to conventionally manufactured samples.

(4) When the beam scan speed decreased from high speed (HS) to low speed (LS), the standard deviation in peak forces of DAH and TLR lattice structures explicitly decreased. It can be explained that samples fabricated with lower scan speed are likely to have fewer random imperfections.

(5) The relationship between the levels of peak forces (Table 5) and micro-porosities (Table 4) is evident in the TLR lattice structure,

which can be easily influenced due to its design with numerous vertical struts. As the micro-porosities increased from 0.02 in HS samples to 0.18 in LS samples, this led to earlier failures of the vertical struts, resulting in a 10 % reduction in reaction forces.

(6) It's important to note that higher KAM values in micro-characterizations indicate that the geometry accumulated more residual stress during the powder bed process. The KAM values explicitly differ between the three geometries in descending order: DAH > TLR > ATC. The presence of higher residual stresses in fabricated structures contributes to earlier strut failures, resulting in lower reaction forces.

(7) However, the residual stresses varied less between samples fabricated with different beam scan speeds (SF, HS, LS) compared to the stresses in different geometries. Therefore, reaction force variations in the same geometry cannot be directly linked to residual stresses.
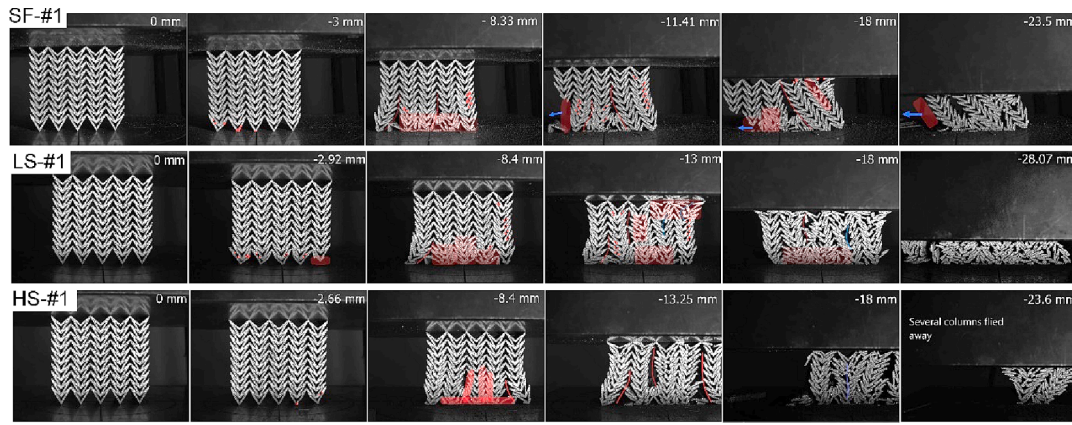
**Fig. 9.** Snapshots at certain times during compressions of DAH lattice structures; samples at each row are SF-#1, LS-#1, and HS-#1, respectively (red points: failed struts, lines: separated lattice column boundaries, red clouds: compressed lattice rows, arrow: sudden separation of uncrushed pieces). (For interpretation of the references to colour in this figure legend, the reader is referred to the web version of this article.)



**Fig. 10.** Snapshots at certain times during compressions of TLR lattice structures: SF-#1, LS-#1, and HS-#1, respectively (red points: failed struts, clouds: crushed lattice rows and regions, arrow: separation of uncrushed/semi-crushed pieces). (For interpretation of the references to colour in this figure legend, the reader is referred to the web version of this article.)
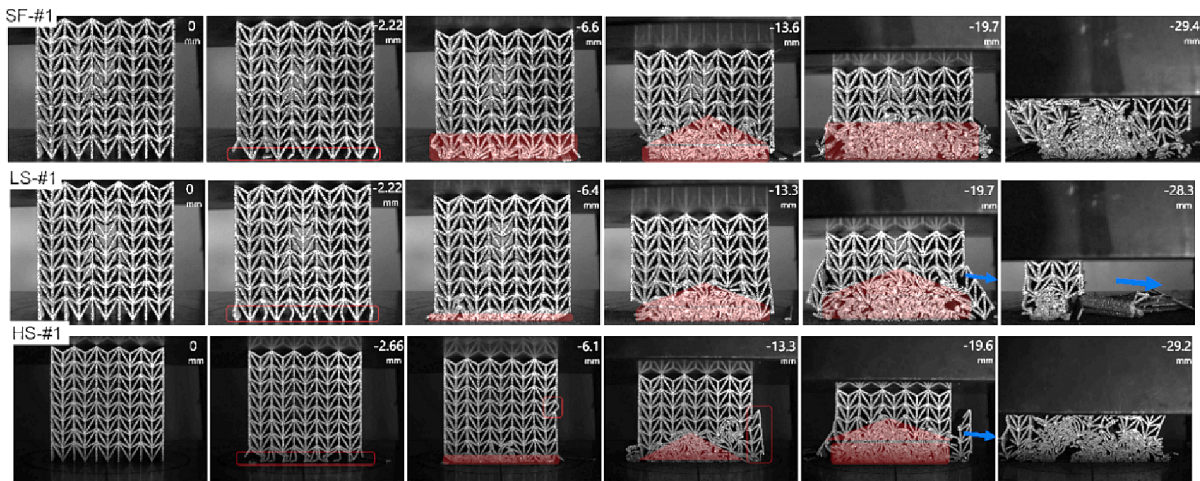
**Table 5**
Peak reaction forces of three different lattice structures, recorded in quasi-static compression tests.

|          | ATC-SF | ATC-HS | ATC-LS | DAH-SF | DAH-HS | DAH-LS | TLR-SF | TLR-HS | TLR-LS |
|----------|--------|--------|--------|--------|--------|--------|--------|--------|--------|
| Avg (kN) | 264.94 | 272.46 | 276.14 | 127.62 | 143.90 | 143.84 | 200.32 | 238.03 | 214.27 |
| Std (kN) | 18.09  | 8.18   | 24.93  | 11.98  | 12.65  | 7.11   | 12.02  | 28.95  | 9.80   |
| Std (%)  | 6.83   | 3.00   | 9.03   | 9.39   | 10.42  | 4.94   | 6.00   | 12.16  | 4.57   |

*3.2.4.2. Specific compressive strength.* Based on the experimental curves of SF type samples, the effective Young modulus in the compression direction was calculated for ATC, DAH, and TLR lattice structures as 1.70, 1.84, and 5.04 GPa, respectively. Additionally, the in-plane Poisson's ratios, obtained until visible plastic deformation phases, ranged roughly between $-0.1$ and $-0.3$ (refer to Fig. S10). As anticipated, stress accumulation led to failures at certain struts, and when struts of small cells came into contact, this resulted in the cutting behavior of negative Poisson's ratio (NPR) due to separations between cells. Owing to the known existence of NPR behavior in the structures, the primary focus of the present work has been on their strength, plastic deformations, and failures.

Compressive strength is a measure of a material's ability to withstand compressive forces before deforming or failing. Specific compressive strength, on the other hand, considers the mass or density of the material, providing a measure of strength relative to its mass or its mass per unit volume. For cellular structures, strength is calculated based on the outermost cross-section using the first peak crushing force. The density for specific strength ($\rho^*$) is relative density and it is determined by multiplying the density of the base material with the relative volume.

$$\sigma^* = \frac{PCF}{A_n m} \text{ or } \sigma^* = \frac{PCF}{A_n \rho^*} \tag{1}$$

Fig. 11-**b** show the specific compressive strength per mass of three different lattice geometries, respectively. The average specific compressive strength of ATC lattice structures outperforms that of DAH and TLR ones by 120 % and %20 (LS samples). Since the three geometries have similar relative volume, mass, and initial contact cross-section, the specific strength relationship between the geometries is the same as the relationship for peak crushing force. When the load-bearing capacity of lattice structures is the main indicator for the
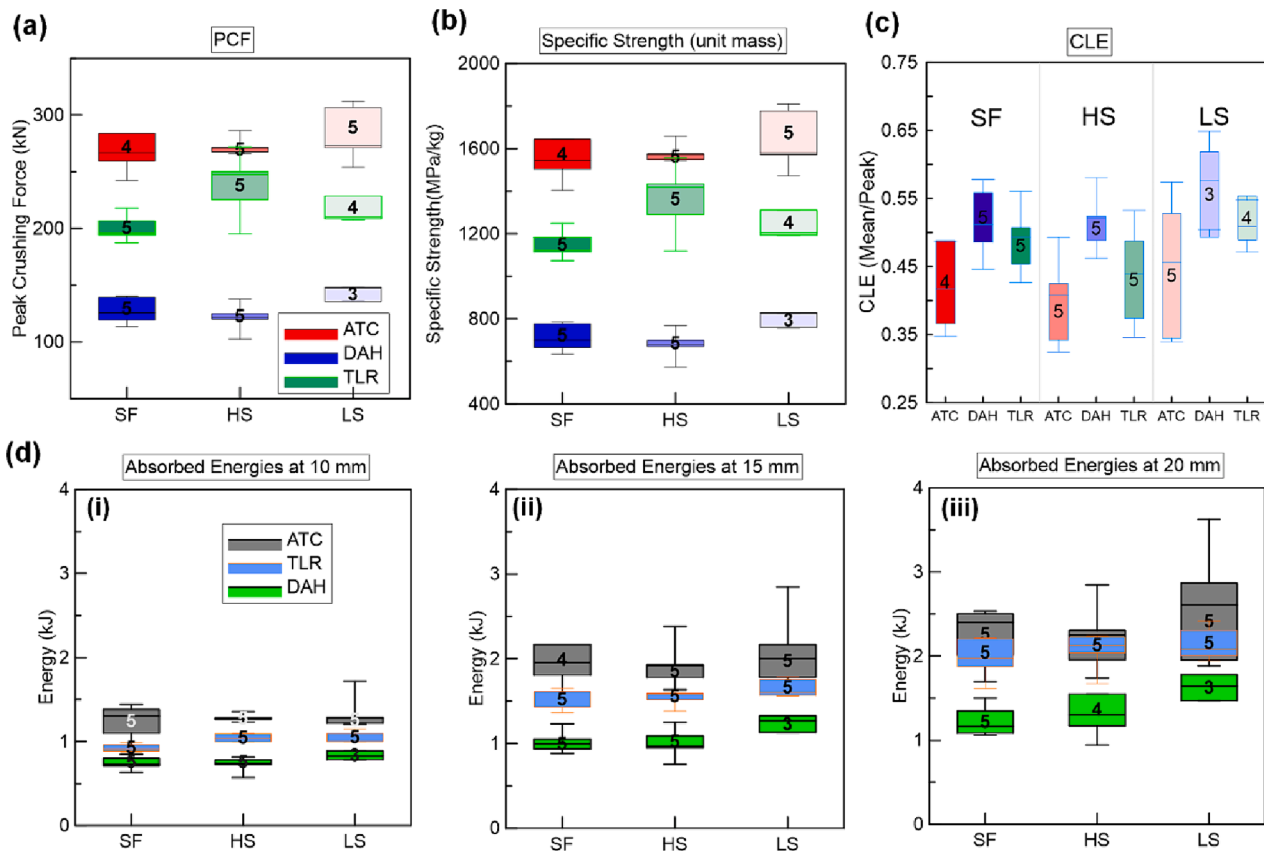
**Fig. 11.** Comparisons of compression response of ATC (black), DAH (green), and TLR (blue) lattice structures in terms of (a) Peak reaction forces (kN), (b) Specific compressive strength (MPa/kg) (c) CLE values (d) Absorbed energies (i) at 10 mm (ii) at 15 mm, (iii) at 20 mm. (For interpretation of the references to colour in this figure legend, the reader is referred to the web version of this article.)

selection, the TLR lattice structure can be the ideal candidate with its low standard deviation of specific compressive strength. Notably, this is also valid for fast production (high beam scan speed) which is highly desired in industrial applications.

*3.2.4.3. Crushing load efficiency (CLE).* In crash scenarios that involve acceleration, the crushing load efficiency (CLE) is utilized as a comparison metric to evaluate the effectiveness of different designs, and determined by calculating the ratio of the mean crushing force (MCF) to the peak crushing force (PCF). Additionally, the alternative calculation can be made based on the nominal stress–strain curve of the lattice structure by dividing plateau stress at a certain point (20 %-30 %) of compression to peak compressive strength. The mean crushing force is obtained by dividing the absorbed energy by the deformation over a specific distance, typically from zero to the reasonable level of the compression (can be earlier of densification region), as depicted on the absorbed energy-deformation curve. CLE is also a critical parameter for occupant protection systems, and Eren et al. [75], clearly show that higher CLE with low PCF tells that after initial peak acceleration towards the impact side, the structure can absorb impact energy during the plateau before the densification point. When the structure is evaluated in terms of nominal stress–strain data, a higher and longer plateau region indicates higher load-bearing capacity under or after impact and failure conditions [76].

$$MCF = \frac{EA}{d} = \frac{1}{d}\int_0^d Fdx \qquad (2)$$

$$CLE = \frac{MCF}{PCF} \qquad (3)$$

In this study, the CLE was calculated using a compression distance of 20 mm. The first reason for choosing this distance is that, during the tests, many crushed pieces did not remain between the platens and were ejected or lost contact with the compression platen. This prevented achieving full densification for all lattice materials. The second reason is that the MCF did not deviate significantly beyond the 20 mm compression level. This holds true even when calculating CLE based on the ratio of plateau stress to the initial peak stress. Consequently, a compression distance of 20 mm (corresponding to 40 % compression, which is 44 % for DAH) was employed for determining CLE. Table 6 presents CLE values with standard deviations. Fig. 11-**c** illustrates the CLE values for three different lattice blocks, which display considerable standard deviation. The primary reason for this deviation is the variability in PCF values. Another contributing factor is the deviation in MCFs, primarily observed in ATC lattice structures.

(1) In terms of CLE values, from highest to lowest, the results are of DAH, TLR, and ATC lattice structures, respectively. Despite that ATC structures exhibited the highest average SEA, they exhibited the lowest average CLE. Noting that, as its standard deviation is high, some ATC samples exhibit high CLE as high as DAH ones.

(2) Noting that standard deviations could reach up to 27.53 % for ATC lattice structures, DAH ones meanwhile reached the highest average CLE due to the lowest PCF they exhibited among the three types of geometries. It means that DAH lattice structures exhibit better load-carrying capacity after impact. (Based on the alternative CLE definition as the ratio of its plateau stress and initial strength.)

(3) However, as shown in Fig. 10, TLR lattice structures exhibit a progressive collapse row by row. Therefore, their 12 % lower CLE

**Table 6**
CLE values of three different lattice structures, based on the quasi-static tests.

|          | ATC-SF | ATC-HS | ATC-LS | DAH-SF | DAH-HS | DAH-LS | TLR-SF | TLR-HS | TLR-LS |
|----------|--------|--------|--------|--------|--------|--------|--------|--------|--------|
| Avg      | 0.417  | 0.409  | 0.426  | 0.512  | 0.522  | 0.577  | 0.494  | 0.439  | 0.509  |
| Std      | 0.070  | 0.085  | 1.17   | 0.066  | 0.059  | 0.072  | 0.067  | 0.093  | 0.038  |
| Std (%)  | 16.67  | 20.72  | 27.53  | 12.85  | 11.38  | 12.53  | 13.56  | 21.27  | 7.54   |

than DAH ones (among LS samples) does not change its being the first choice.

(4) Reminding that as the ATC and TLR lattice structures exhibited the highest average specific compressive strength, at higher loads that DAH ones cannot withstand, they are superior solutions for the load-carrying capacity after compression damage.

(5) Additionally, similar to the case of SEA values, LS type samples of all types of geometries exhibited the highest average CLE values.

*3.2.4.4. Specific energy absorption (SEA).* Fig. 11-d displays the absorbed energies for each geometry. While anti-tetrachiral lattice structures had the highest energy absorption in all samples, TRL lattice structures (the stiffer version of DAH lattice structures) were able to dissipate more energy than DAH ones. Although absorbed energies at the initial stages of compression were similar across all repeats in each geometry, force deviations became distinct at subsequent steps at 15 mm and 20 mm compressions due to different deformation patterns of the geometries built with varying manufacturing parameters (scan speed). If the main requirement is lightweight and high energy absorption, the indicator of specific energy absorption (SEA, **Eq. (4)**), which is the energy absorbed per unit mass, is used to evaluate the effectiveness of the designs and aims to increase the energy absorption per unit mass for structures.

$$SEA = \frac{\int_0^d F(x)dx}{m} \tag{4}$$

In foam compressions, 40–50 % densification is typically reasonable, and visual observations during the current additively manufactured sample tests suggest that a similar assumption holds correct. Since several non-compressed pieces remained in the samples, particularly after compressions of 20–25 mm, only cases up to 20 mm were taken into consideration. Table 7 presents the SEA for each geometry.

Briefly, results indicate that three topologies exhibited different compression responses due to: 1- Geometry oriented reasons (e.g, stretch or/and bending dominated deformation mechanisms), 2- Material induced reasons (e.g. brittle compression causes earlier failures than polymers), 3- Manufacturing induced reasons (e.g., changing scanning

speed or type changes stress in parts or process inherently leaves defects on the parts). Although stretch-dominated motion generally favours higher energy absorption [77], bending-dominated polymer ATC lattice structures reportedly outperformed stretch-dominated polymer re-entrant lattice structures [33]. Re-entrant topology is not favourable for energy absorption [78]. In this aspect, findings in the present study confirms ATC topology's position compared to DAH and TLR exhibiting stretch-dominated compressions. Researchers recently reported that additively manufactured metal lattice structures do not fit in the Gibson-Ashby bending versus stretch (axial deformation) dominated deformations [79] due to complex modes and failures related with the PBF process based imperfections during deformations [80–82]. In addition to effect of topology (1#) itself, present study featured effect of material (#2) and manufacturing (#3) oriented reasons. For instance, superior energy absorptions with polymeric composite DAH lattice structures [35] and their progressively collapse of rows have not been matched with present findings for Ti64 DAH structures. Reminding that potentially weak or strain-sensitive inter - lattice column regions of DAH structure, separated earlier without crushing, cause less energy absorption than expected (Fig. 9). Two reasons were identified such as low failure strain with imperfections and the highest residual stress among three topologies (KAM values in Table 4) that are indicatives for effect of material selection (Ti64) and the powder bed process, respectively. Important to note that, during phase transformation (β → α) there was no significant α selection depending on model and/ or scan speed. When the geometry changes (ATC, DAH, TLR), during the PBF-EB process, single or multiple scans can happen at different sections, and this causes porosities and residual stresses at different amounts. Imperfection struts populated zones change if the design has vertical, horizontal, or complex shape cells.

(1) The results indicate that DAH lattice structures with LS speed had 32 % and 28 % higher SEA than samples built with SF and HS samples, respectively. TLR lattice structures with LS speed had 12.2 % and 6.2 % higher SEA than samples built with speed function (SF) and high scan speed (HS) samples, respectively.

**Table 7**
SEA values at compressions of 10 mm, 15 mm, and 20 mm in quasi-static tests.

| **10 mm compression** | | | | | | | | | |
|-----------------------|--------|--------|--------|--------|--------|--------|--------|--------|--------|
|             | ATC-SF | ATC-HS | ATC-LS | DAH-SF | DAH-HS | DAH-LS | TLR-SF | TLR-HS | TLR-LS |
| Avg (kJ/kg) | 9.19   | 9.29   | 9.04   | 5.21   | 5.08   | 5.84   | 6.69   | 7.56   | 7.69   |
| Std (kJ/kg) | 1.59   | 0.32   | 1.54   | 0.58   | 0.66   | 0.37   | 0.36   | 0.36   | 0.55   |
| Std (%)     | 17.32  | 3.46   | 17.07  | 11.19  | 12.97  | 6.38   | 5.39   | 4.72   | 7.14   |

| **15 mm compression** | | | | | | | | | |
|-----------------------|--------|--------|--------|--------|--------|--------|--------|--------|--------|
|             | ATC-SF | ATC-HS | ATC-LS | DAH-SF | DAH-HS | DAH-LS | TLR-SF | TLR-HS | TLR-LS |
| Avg (kJ/kg) | 13.69  | 13.96  | 13.85  | 7.15   | 7.02   | 8.71   | 10.85  | 11.14  | 12.08  |
| Std (kJ/kg) | 2.30   | 2.03   | 3.31   | 0.93   | 1.29   | 0.71   | 0.92   | 0.68   | 0.88   |
| Std (%)     | 16.81  | 14.53  | 23.89  | 13.07  | 18.45  | 8.11   | 8.48   | 6.09   | 7.31   |

| **20 mm compression** | | | | | | | | | |
|-----------------------|--------|--------|--------|--------|--------|--------|--------|--------|--------|
|             | ATC-SF | ATC-HS | ATC-LS | DAH-SF | DAH-HS | DAH-LS | TLR-SF | TLR-HS | TLR-LS |
| Avg (kJ/kg) | 15.64  | 16.08  | 16.86  | 8.63   | 8.93   | 11.43  | 14.31  | 14.91  | 15.84  |
| Std (kJ/kg) | 2.75   | 3.03   | 5.18   | 1.32   | 1.90   | 1.07   | 1.81   | 1.67   | 1.54   |
| Std (%)     | 17.6   | 18.83  | 30.74  | 15.26  | 21.24  | 9.41   | 12.62  | 11.20  | 9.75   |

When scan speed varied (SF, HS, and LS) to manufacture the lattices, SEA values increased more in DAH lattice structures compared to ATC and TLR ones.

(2) For 20 mm compressions, ATC (LS) lattice structures had 47.5 % and 6.44 % higher SEA (kJ/kg) than that of DAH (LS) and TLR (LS) ones, respectively.

(3) As compression progressed from 10 mm to 20 mm, the standard deviations for SEAs also increased for the three different geometries.

(4) Furthermore, TLR lattice structures exhibited SEA values with the lowest standard deviations in the range of 9.75 %-12.62 % while ATC ones exhibited SEA values with the highest standard deviations in the range of 17.6–30.4 % in the compression tests.

(5) It's worth reminding that deployed residual stresses, as indicated by the KAM data in Table 5, during the PBF-EB process, follow an ascending order: ATC < TRL < DAH. High residual stresses, when present, can lead to premature failures at the struts, causing failures earlier than intended by the design. For instance, in DAH lattice structures, an early separation between cell columns, resulting in reduced energy absorption, can be mitigated by eliminating these residual stresses. Additionally, eliminating residual stresses can contribute to ensuring that all compressed lattices remain intact during compression, increasing the SEA for all geometries, as some pieces will not detach without undergoing crushing.

(6) Another outcome for TLR lattice structures, which is the reinforced version of DAH lattice structures with vertical struts, is that residual stress was distributed to these reinforcing struts at the unit cell level. Since energy absorption performance is primarily influenced by geometrical parameters, such as the presence of more struts contributing to higher energy absorption, fabricating lattices with more struts can result in lower residual stress at each strut, subsequently contributing to progressive collapse. TLR structures exhibited higher SEA owing to vertical struts which provide strengthening mechanisms between columns and progressive collapse which are the problem of DAH.

(7) The lowest residual stress in ATC lattice structures contributes to its highest energy absorption, in line with its geometry, creating the highest in-plane strength. However, the large standard deviation in the energy absorption for all scan types requires more attention to its complex design with many short struts and hollow ligaments compared to the other two designs. The low microporosity in measurements (ATC SF: 0.08, HS: 0.07, LS: 0.08) and low KAM values for residual stresses (ATC SF: 0.71, HS: 0.66, LS: 0.65) likely do not cause fluctuations in energy absorptions. This is possibly related to its complex geometry initiating many different failure paths, as also observed in compression patterns, where many local bucklings and failures occur, different from DAH and TLR lattice structures. While the ATC's horizontal struts transfer loads, and tend to rotate around edge hollow elements, resisting bending, its short vertical struts tend to withstand high in-plane loads. the design with vertical struts under a critical length against Euler buckling, presents promising energy absorption and load bearing capacity as it distributed loads as fractures and small failures at unit cells. As a design having the lowest residual stress among three designs requires attention because high residual stress could cause earlier failures decreasing SEA. Eliminating potential defects at struts can enhance energy absorption performance by increasing mean crushing force (or plateau stress) after the highest initial peak force of the structure.

(8) Large fluctuations in specific energy absorptions of ATC lattice structures make TLR lattice structures favorable (ATC-LS: 16.86 kJ/kg with std30.74 % vs TLR-LS:15.84 kJ/kg with std9.75 %) in product applications, as they exhibit low standard deviations.

## 3.3. Numerical analyses

### 3.3.1. Peak crushing forces (PCF)

To compare the experiments and finite element analyses, the data from the SF group were utilized, as shown in Fig. 14(i) sub-figures. It is crucial to remember that despite there are variations between the results of compressions of the LS, HS, and SF samples (peak force, energy), only the SF ones with three curves were employed to follow the coherence between the FEA curves and compression experiments in a simplified manner. The finite element analyses successfully captured the initial peak force of the ATC lattice structures, closely matching the experimental results (analysis: 240 kN, SF experiments: between 265 and 276 kN). However, when it came to the numerical analysis of the DAH structures, it failed to replicate both the magnitude and timing of the initial peaks observed in the experiments, which ranged from 128 to 144 kN. Calibration through multiple trials may be necessary to achieve a better match in the level and timing of the peak force between numerical predictions and experiments. Similarly, the TLR structures exhibited a 245 kN response in the analyses, whereas the SF samples in the experiments showed an average initial peak reaction of 200 kN. However, TLR-HS samples exhibited a higher average peak force of 238 kN in the compression experiments (Fig. 10-c (iii)), which is very close to the numerical predictions. For TLR structures, the disparity in the level of the peak reactions between the analyses and compression experiments can be attributed to random imperfections in the vertical struts resulting from the PBF process (e.g., less residual stress at vertical struts in HS samples helped to capture close peaks to FEA).

Another point to consider is the subsequent force curve formation after the initial peaks. Each structure exhibited unique compressive strength levels in the plateau region. The ATC structures have a numerical reaction force formation starting densification earlier than the experimental curves. Numerical formations of DAH and TLR structures were coherent with the experiments. For instance, peak formations (three ordered peaks due to compressions of cell rows) of TLR structures were captured in numerical analyses. DAH structures numerically exhibited an initial first peak and subsequent fluctuations close to each other, as observed in the experiments. In summary, when dealing with responses from cellular materials with highly fluctuating force behavior, SEA curves or mean crushing force curves can serve as better comparison tools. The MCF curves (Supp. Fig. S9) show that the experimental and numerical mean crushing force exhibit consistency. Although the numerical deformation patterns exhibit a similar response to experiments, the force curve does not precisely match the shape of the experimental data due to undiscovered many imperfections inside the struts.

### 3.3.2. Specific energy absorption (SEA)

Fig. 12 (ii) sub-figure presents strong agreement between the experimental and numerical results of SEAs. Although there is incoherence in the force curve for the DAH structures, their SEA values closely match the experimental curves. The force peaks of the ATC and TLR lattices output with higher levels, and these were reflected in the energy curves as higher values, yet they remain within acceptable boundaries.

### 3.3.3. Deformation patterns

Verification of the experimental deformation modes requires the introduction of imperfections at specific locations. Reminding that ATC lattice structures exhibited V or diagonal-shaped shear bands. Fig. 13-a shows that in the numerical verification, a similar V shear band was obtained, with comparable peak crushing force and SEA values. From the stress map, critical stress locations are the regions where top–bottom neighboring cells touch each other. However, it is required to simulate visible local failures around hollow edge elements during the early phase of experimental compressions, as these locations likely contain imperfections.
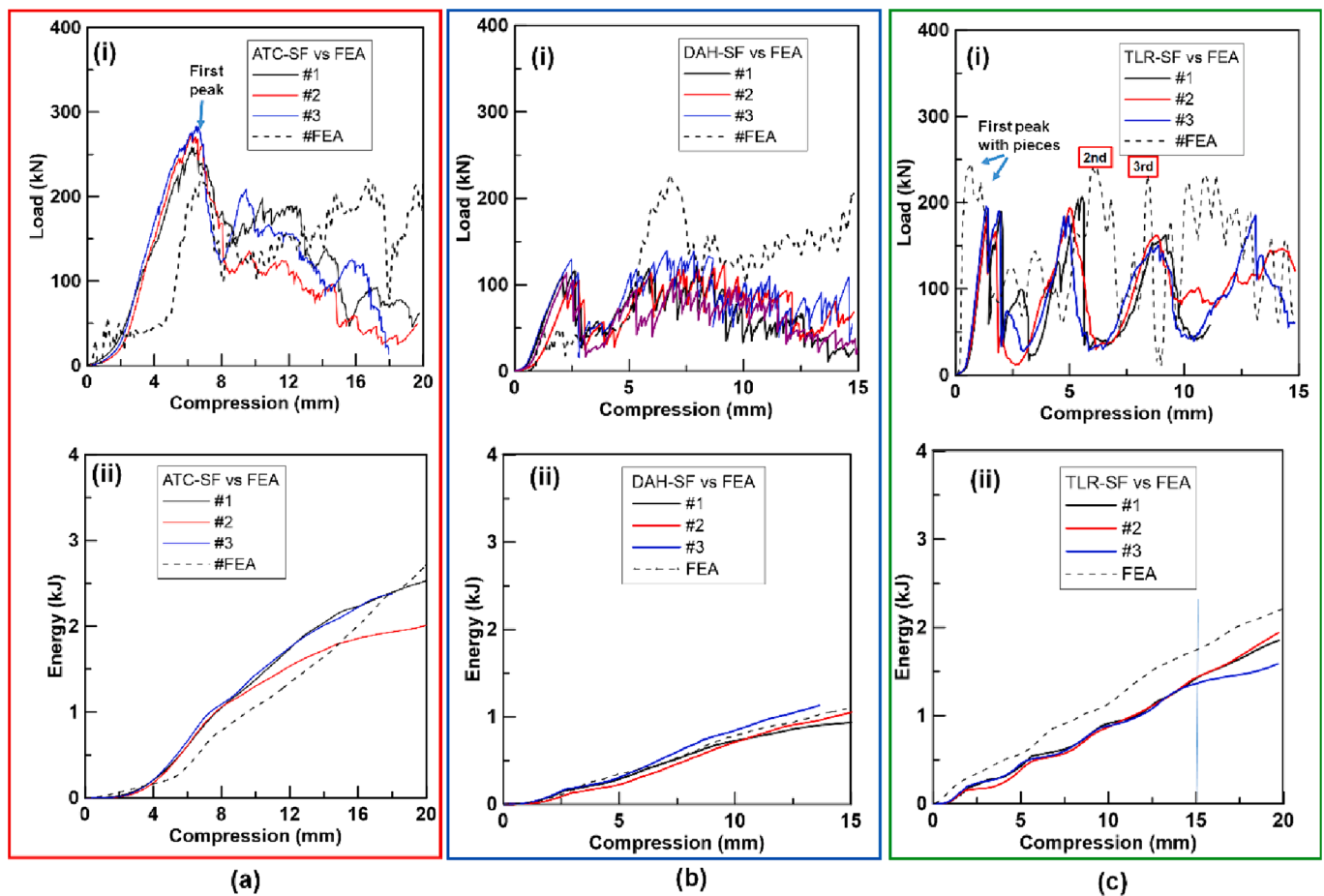
**Fig. 12.** Comparison of experimental and numerical (i) reaction load-compression and (ii) absorbed energy-compression curves of (a) ATC, (b) DAH, and (c) TLR lattice blocks (three test repetitions of 0 deg-SF samples).

The DAH ones exhibited compression at the bottom, then separation between columns. Both were captured at numerical analyses. Critically, the weak bond strength between columns was introduced through material data. Fig. 13-b shows that after separation between columns, the highest stress occurred at top struts of unit cells due to axial compression (stretch dominated motion), and these separated between each other as in the experiments. Notably, TLR lattice structures displayed a step-by-step collapse, commencing from the bottom row of the structures during the experiments. This behavior was accurately captured in numerical analyses. However, it's worth noting that in the experimental data, the reaction force curves showed prolonged stays at lower levels after each peak decline. The stress map in Fig. 13-c reveals that vertical struts experience the highest stress, aligning with expectations. Even during the subsequent foldings of rows, the 'v' shape struts experience very low stresses. Therefore, designs featuring thinner V struts that do not cause Euler buckling have the potential to enhance SEA. To sum up, Fig. 13 shows obtained deformation modes in the Abaqus explicit solver, indicating that initial failure modes such as V band formation in ATC lattices, initial compression, and separation between columns in DAH lattices and initial collapse location and progressive collapse mechanism in TLR lattices successfully predicted.

### 3.4. Outlook

In addition to the comparison in section 3.2, this section provides an outlook using SEA values found in the literature for in-plane compressions. Fig. 14 visually represents the 2D lattice structures in our study, comparing them to previous compression studies using a specific energy versus density plot. The density at x-axis represents the product of the

base material density and relative volume. The density at x-axis is also named apparent density.

Polymeric square hierarchical honeycombs 6 kJ/kg [83], conventionally manufactured Aluminum 6061 tetrahedral lattice structures with 30 kJ/kg [84]. PBF-L process and AlSi10Mg alloy based double gyroid lattice structures with 24.32 kJ/kg [85] are low density examples in the figure. PBF process and Ti64-based 3D lattice structures exhibiting high SEAs are listed as follows: FCCZ-type (65 kJ/kg) [86], functionally graded 3D Honeycomb (33.3 kJ/kg) [87] and Diamond TPMS structures (53 kJ/kg) [88]. Steel 304 material 3D MBCC-type lattice structures had a lower SEA of 9 kJ/kg compared to other 3D types [89]. SS 316L plate lattice structures could absorb 14.65 kJ/kg (0.5 strain), which is 30 % higher than the block with Ti64 base material, due to early fractures at Ti64 material [90]. In the realm of 3D auxetic structures, SS 316L 3D re-entrant lattice structures demonstrated superior performance with SEA of 106 kJ/kg [91]. In contrast, a design of Ti64 3D ATC lattice structures had a low SEA of 4.5 kJ/kg, indicating that this version of 3D ATC lattices may not be sufficient for energy absorption [92]. However, in the case of 2D lattice structures, lower SEAs are generally expected and a comparison among 2D designs is more logical for in-plane compressions. There are also data of conventionally manufactured AL-5052 hexagonal honeycomb [93] and 304 SS corrugated [94] lattice structures which exhibited low SEAs within relatively low densities, in the plot. PBF-L and 316L steel based thickened wall hexagonal honeycomb structures with 15.8 kJ/kg for a relatively high relative volume (0.86) [95] and Steel 304 based Miora (origami-inspired) and re-entrant lattice structures with 7.83 kJ/kg and 6.18 kJ/kg [38], respectively. To the best of our knowledge, the present study is the first to report the compression of Ti64 material 2D DAH, TLR, and ATC lattice structures, resulting in SEAs
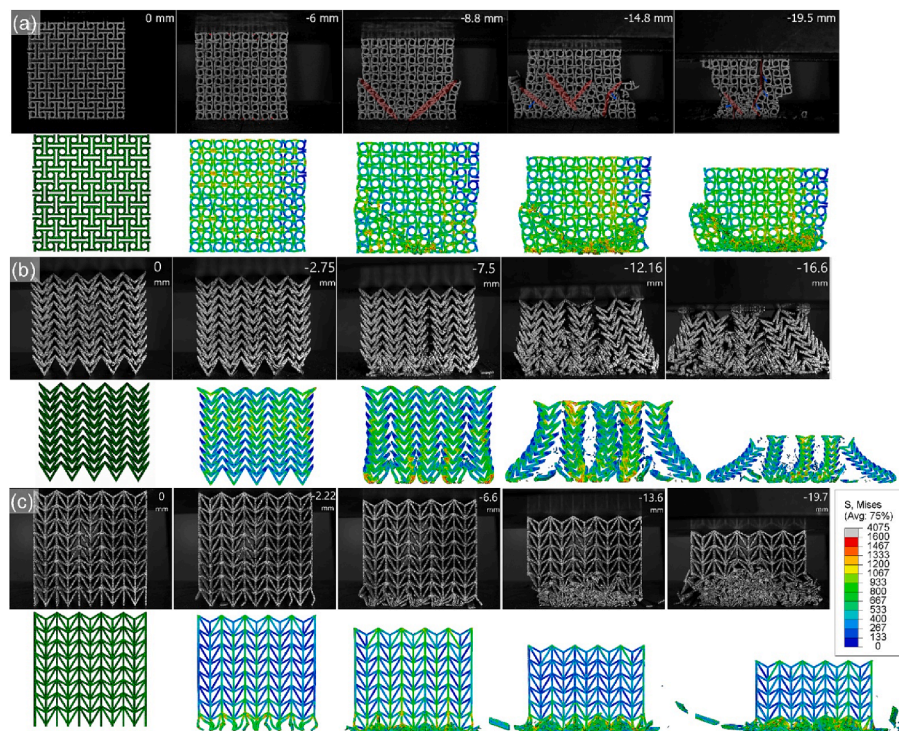
**Fig. 13.** Comparison of compression deformation modes in the experimental and numerical analyses of (a) ATC, (b) DAH, and (c) TLR lattice structures (SF type samples), respectively. (For interpretation of the references to colour in this figure legend, the reader is referred to the web version of this article.)

of 11.43 kJ/kg, 14.31 kJ/kg, and 15.64 kJ/kg, respectively, at 0.4 strain. It's worth noting that the SEA could potentially increase if the failure strain or elongation of the Ti64 base material were enhanced (employing material with a higher ductility). Because early failures and non-crushed separation of columns decreased the absorbed energy during the tests. Further tests with the design variations having less relative volume (e.g., reduced wall thickness) can contribute to identifying other early failure problems (e.g., geometry effect, residual stress or dense defect regions at struts). Then, the critical points in the design with a less relative volume (or apparent density) can be improved to have a close SEA to 3D lattice structures.

## 4. Conclusion

In this study, a novel combination for the in-plane quasi-static compression behavior of 2D lattice structures was investigated. This was achieved by utilizing (i)- Ti6Al4V material, (ii)- specific 2D auxetic lattice designs, and (iii)- PBF-EB process at various scan speeds. The vast majority of the literature has considered 2D-type lattice structures for polymeric materials, confirming enhanced in-plane compression behavior of polymeric re-entrant and DAH auxetic structures. To the best of the authors' knowledge, this study is the first to conduct a comparison between three promising auxetic structures with Ti64 material at various manufacturing speeds, focusing on specific energy absorptions (SEA). In this aspect, the findings contribute to developing cellular structures in multifunctional applications with secondary employment for efficient cooling channels at high-temperature sections. The following conclusions were drawn:

(i) 2D ATC lattice structures built with low scan speed (ATC's LS Group) are the samples that exhibited the highest SEA, outperforming DAH and TLR lattice structures by 47.5 % and 6.44 %, respectively. While the double arrow design exhibited weaknesses between cells, a reinforced/stiffer version of it, the tree-like re-entrant lattice structures, can achieve higher SEA by 39 % (at 20 mm deflection). As TLR structures exhibited SEA close to

that of anti-tetrachiral designs with the lowest standard deviation, they can be preferred in industrial-scale applications. A large standard deviation in results is not desired particularly for the mission-critical applications. The tests showed that evaluating the crushing performance of Ti64 lattice structures requires conducting numerous tests due to the variations in results depending on the type of lattice geometry. Additionally, deformation observations during the repetitive tests can help identify critical locations for improving against imperfections.

(ii) Manufacturing speed (beam scan speed in PBF-EB) plays a critical role in energy absorption variations. When it decreased, SEAs in compression tests increased significantly in DAH (by up to 32 %) and TLR (by up to 12 %) lattice structures. While TLR lattice structures exhibited the lowest average standard deviations (SF, HS, LS types) in results, ATC lattice structures exhibited the highest one (up to 30.7 %). It was reasoned that random imperfections in ATC cells are more influential than the effect of scan speed.

(iii) It is a critical finding for 2D Ti64 lattice structures that deployed residual stress varies based on the geometry. Accumulated varying levels of residual stresses during the manufacturing are in the descending order of DAH, TLR, and ATC, which inversely correlates with the SEAs. This contributes to their exhibiting the highest energy absorption, in line with their geometry, creating the highest in-plane strength. On the other hand, the effect of the imperfections on the reaction forces, while decreasing microporosity in struts, increased the energy absorption of DAH lattice structures, however, it is not decisive for TLR ones. Reduced micro porosity levels increased the peak reaction force (or specific compressive strength) of TLR lattice structures due to their design with populated vertical struts. When faster fabrication is crucial in the manufacturing of many samples due to cost-effectiveness and time limits in projects, high beam scan speed can be preferred with a known performance difference that varies according to the type of lattice geometry. For instance, the higher SEA of 6.2 % in TLR's LS samples compared to HS samples may be
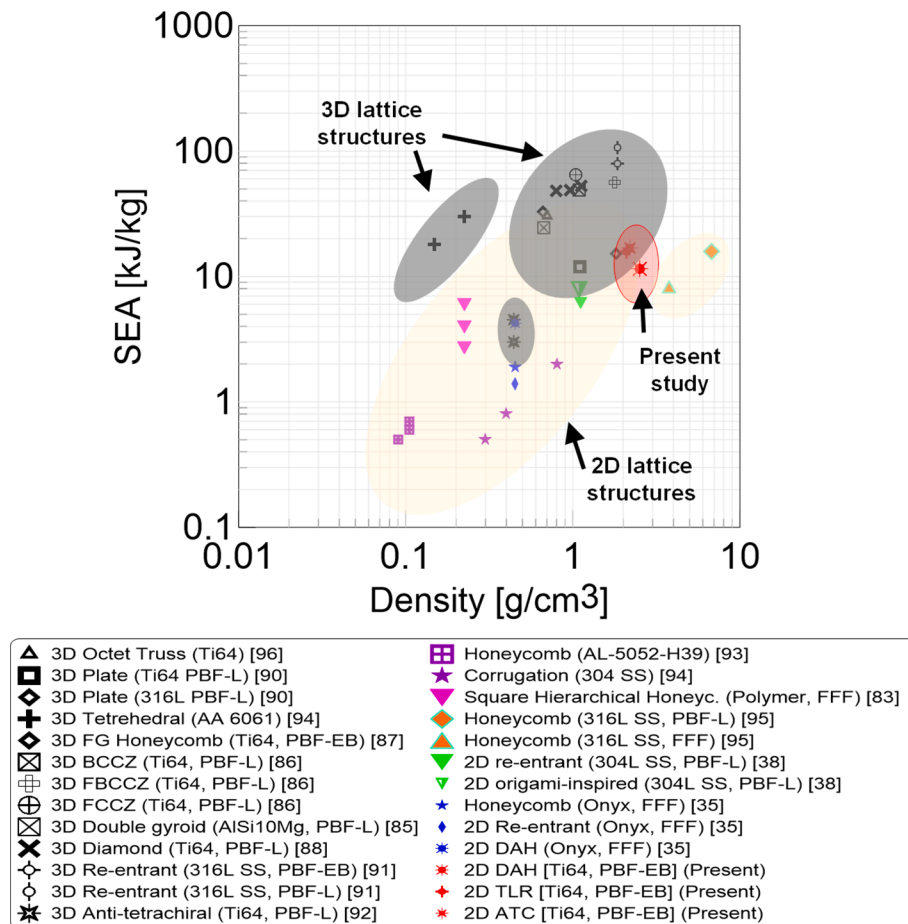
**Fig. 14.** SEA comparison of present work with the different lattice geometries in the literature for in-plane compression [35,38,83–96].

disregarded in an industrial setting, considering its fourfold acceleration of the manufacturing process.

(iv) Major deformation modes of all lattice structures were captured in numerical analyses through imperfections introduced based on the observation of the experiments. However, peak reaction forces were not accurately estimated numerically due to complex geometries with many imperfections in the manufactured samples, which proposed the need for CT scan data input for future studies.

In summary, for future studies focusing on 2D mechanical metamaterials, the compression deformation of blocks with lower relative volumes, approximately 25 % or less, and the required optimum PBF-EB process conditions should be investigated. This includes aiming for lower residual stress levels and fewer imperfections in thinner struts, such as 0.4–0.6 mm. Such efforts will also help reduce the number of uncrushed pieces separating during compression tests. Moreover, it can be proposed to utilize micro-CT scan data in the finite element analyses of the compression of vertical beams can contribute to accurately obtaining peak reaction forces. Such a study requires smaller and simpler geometries with vertical struts.

## CRediT authorship contribution statement

**Zana Eren:** Writing – original draft, Visualization, Validation, Methodology, Investigation, Formal analysis, Data curation, Conceptualization. **Ozkan Gokcekaya:** Writing – review & editing, Writing – original draft, Visualization, Validation, Methodology, Investigation,

Formal analysis, Data curation, Conceptualization. **Demet Balkan:** Writing – review & editing, Project administration, Funding acquisition, Data curation. **Takayoshi Nakano:** Writing – review & editing, Supervision, Resources, Project administration, Funding acquisition. **Zahit Mecitoğlu:** Writing – review & editing, Supervision, Resources, Project administration, Funding acquisition.

## Declaration of competing interest

The authors declare that they have no known competing financial interests or personal relationships that could have appeared to influence the work reported in this paper.

## Data availability

Data will be made available on request.

## Acknowledgments

## Appendix A. Supplementary data

Supplementary data to this article can be found online at https://doi.org/10.1016/j.matdes.2024.112885.

## References

[1] R. Lakes, Foam structures with a negative poisson's ratio, Science 235 (1987) 1038–1040.

[2] X. Yu, J. Zhou, H. Liang, Z. Jiang, L. Wu, Mechanical metamaterials associated with stiffness, rigidity and compressibility: a brief review, Prog. Mater. Sci. 94 (2018) 114–173.

[3] F.L. Scarpa, F. Dallocchio, M. Ruzzene, Identification of acoustic properties of auxetic foams, SPIE, in, 2003, pp. 468–474.

[4] X. Hou, Z. Deng, J. Zhou, Symplectic analysis for the wave propagation properties of conventional and auxetic cellular structures, Int J Numer Anal Model 2 (2011) 298–314.

[5] H.R. Joshi, Finite Element Analysis of effective mechanical properties, vibration and acoustic performance of auxetic chiral core sandwich structures, (2013).

[6] M. Ghafouri, M. Ghassabi, M.R. Zarastvand, R. Talebitooti, Sound propagation of three-dimensional sandwich panels: influence of three-dimensional re-entrant auxetic core, AIAA J. 60 (2022) 6374–6384.

[7] L. Ma, Y.-L. Chen, J.-S. Yang, X.-T. Wang, G.-L. Ma, R. Schmidt, K.-U. Schröder, Modal characteristics and damping enhancement of carbon fiber composite auxetic double-arrow corrugated sandwich panels, Compos. Struct. 203 (2018) 539–550.

[8] Y.-L. Chen, D.-W. Wang, L. Ma, Vibration and damping performance of carbon fiber-reinforced polymer 3D double-arrow-head auxetic metamaterials, J. Mater. Sci. 56 (2021) 1443–1460.

[9] Z. Tao, X. Ren, L. Sun, Y. Zhang, W. Jiang, A.G. Zhao, Y.M. Xie, A novel re-entrant honeycomb metamaterial with tunable bandgap, Smart Mater. Struct. 31 (2022) 095024.

[10] J. Sun, H. Gao, F. Scarpa, C. Lira, Y. Liu, J. Leng, Active inflatable auxetic honeycomb structural concept for morphing wingtips, Smart Mater. Struct. 23 (2014) 125023.

[11] T. Fey, F. Eichhorn, G. Han, K. Ebert, M. Wegener, A. Roosen, K. Kakimoto, P. Greil, Mechanical and electrical strain response of a piezoelectric auxetic PZT lattice structure, Smart Mater. Struct. 25 (2015) 015017.

[12] P. Budarapu, Y.B. Sudhir Sastry, R. Natarajan, Design concepts of an aircraft wing: composite and morphing airfoil with auxetic structures, Front. Struct. Civ. Eng. 10 (2016) 394–408.

[13] Z. Chen, X. Wu, Z. Wang, J. Shao, Concepts for morphing airfoil using novel auxetic lattices, Springer, in, 2020, pp. 265–274.

[14] K.K. Dudek, J.A.I. Martínez, G. Ulliac, M. Kadic, Micro-scale auxetic hierarchical mechanical metamaterials for shape morphing, Adv. Mater. 34 (2022) 2110115.

[15] S.C. Ugbolue, Y.K. Kim, S.B. Warner, Q. Fan, C.-L. Yang, O. Kyzymchuk, Y. Feng, The formation and performance of auxetic textiles. Part I: theoretical and technical considerations, J. Text. Inst. 101 (2010) 660–667.

[16] T. Lim, A. Alderson, K. Alderson, Experimental studies on the impact properties of auxetic materials, Phys. Status Solidi B 251 (2014) 307–313.

[17] S. Yang, C. Qi, D. Wang, R. Gao, H. Hu, J. Shu, A comparative study of ballistic resistance of sandwich panels with aluminum foam and auxetic honeycomb cores, Adv. Mech. Eng. 5 (2013) 589216.

[18] Y. Hou, R. Neville, F. Scarpa, C. Remillat, B. Gu, M. Ruzzene, Graded conventional-auxetic kirigami sandwich structures: flatwise compression and edgewise loading, Compos. Part B Eng. 59 (2014) 33–42.

[19] C. Yang, H.D. Vora, Y. Chang, Behavior of auxetic structures under compression and impact forces, Smart Mater. Struct. 27 (2018) 025012.

[20] G. Imbalzano, P. Tran, T.D. Ngo, P.V. Lee, Three-dimensional modelling of auxetic sandwich panels for localised impact resistance, J. Sandw. Struct. Mater. 19 (2017) 291–316.

[21] S. Hou, T. Li, Z. Jia, L. Wang, Mechanical properties of sandwich composites with 3d-printed auxetic and non-auxetic lattice cores under low velocity impact, Mater. Des. 160 (2018) 1305–1321.

[22] C. Qi, A. Remennikov, L.-Z. Pei, S. Yang, Z.-H. Yu, T.D. Ngo, Impact and close-in blast response of auxetic honeycomb-cored sandwich panels: Experimental tests and numerical simulations, Compos. Struct. 180 (2017) 161–178.

[23] A. Ingrole, A. Hao, R. Liang, Design and modeling of auxetic and hybrid honeycomb structures for in-plane property enhancement, Mater. Des. 117 (2017) 72–83.

[24] Q. Gao, X. Zhao, C. Wang, L. Wang, Z. Ma, Multi-objective crashworthiness optimization for an auxetic cylindrical structure under axial impact loading, Mater. Des. 143 (2018) 120–130.

[25] G. Imbalzano, S. Linforth, T.D. Ngo, P.V.S. Lee, P. Tran, Blast resistance of auxetic and honeycomb sandwich panels: Comparisons and parametric designs, Compos. Struct. 183 (2018) 242–261.

[26] X. Ren, R. Das, P. Tran, T.D. Ngo, Y.M. Xie, Auxetic metamaterials and structures: a review, Smart Mater. Struct. 27 (2018) 023001.

[27] W. Wu, W. Hu, G. Qian, H. Liao, X. Xu, F. Berto, Mechanical design and multifunctional applications of chiral mechanical metamaterials: a review, Mater. Des. 180 (2019) 107950.

[28] Y. Ma, F. Scarpa, D. Zhang, B. Zhu, L. Chen, J. Hong, A nonlinear auxetic structural vibration damper with metal rubber particles, Smart Mater. Struct. 22 (2013) 084012.

[29] M. Ranjbar, L. Boldrin, F. Scarpa, S. Neild, S. Patsias, Vibroacoustic optimization of anti-tetrachiral and auxetic hexagonal sandwich panels with gradient geometry, Smart Mater. Struct. 25 (2016) 054012.

[30] Q. Li, D. Yang, Vibration and sound transmission performance of sandwich panels with uniform and gradient auxetic double arrowhead honeycomb cores, Shock Vib. 2019 (2019).

[31] R.P. Bohara, S. Linforth, T. Nguyen, A. Ghazlan, T. Ngo, Anti-blast and-impact performances of auxetic structures: a review of structures, materials, methods, and fabrications, Eng. Struct. 276 (2023) 115377.

[32] K. Günaydın, Z. Eren, F. Scarpa, Experimental investigation of auxetic structures subjected to quasi static axial load, in, 8th int. conf. recent adv. space technol, RAST, IEEE 2017 (2017) 7–10.

[33] K. Günaydın, Z. Eren, Z. Kazancı, F. Scarpa, A.M. Grande, H.S. Türkmen, In-plane compression behavior of anti-tetrachiral and re-entrant lattices, Smart Mater. Struct. 28 (2019) 115028, https://doi.org/10.1088/1361-665X/ab47c9.

[34] T. Li, F. Liu, L. Wang, Enhancing indentation and impact resistance in auxetic composite materials, Compos. Part B Eng. 198 (2020) 108229, https://doi.org/10.1016/j.compositesb.2020.108229.

[35] J. Zhou, H. Liu, J.P. Dear, B.G. Falzon, Z. Kazancı, Comparison of different quasi-static loading conditions of additively manufactured composite hexagonal and auxetic cellular structures, Int. J. Mech. Sci. 244 (2023) 108054, https://doi.org/10.1016/j.ijmecsci.2022.108054.

[36] G. Chen, Y. Cheng, P. Zhang, J. Liu, C. Chen, S. Cai, Design and modelling of auxetic double arrowhead honeycomb core sandwich panels for performance improvement under air blast loading, J. Sandw. Struct. Mater. 1099636220935563 (2020).

[37] J.X. Qiao, C.Q. Chen, Impact resistance of uniform and functionally graded auxetic double arrowhead honeycombs, Int. J. Impact Eng. 83 (2015) 47–58, https://doi.org/10.1016/j.ijimpeng.2015.04.005.

[38] Q. Li, X. Zhi, F. Fan, Quasi-static compressive behaviour of 3D-printed origami-inspired cellular structure: experimental, numerical and theoretical studies, Virtual Phys. Prototyp. 17 (2022) 69–91.

[39] Y.J. Chen, F. Scarpa, Y.J. Liu, J.S. Leng, Elasticity of anti-tetrachiral anisotropic lattices, Int. J. Solids Struct. 50 (2013) 996–1004.

[40] M.-F. Guo, H. Yang, L. Ma, Design and analysis of 2D double-U auxetic honeycombs, Thin-Walled Struct. 155 (2020) 106915.

[41] Y. Gao, Q. Wu, X. Wei, Z. Zhou, J. Xiong, Composite tree-like re-entrant structure with high stiffness and controllable elastic anisotropy, Int. J. Solids Struct. 206 (2020) 170–182.

[42] R. Jafari Nedoushan, Y. An, W.-R. Yu, M.J. Abghary, Novel triangular auxetic honeycombs with enhanced stiffness, Compos. Struct. 277 (2021) 114605, https://doi.org/10.1016/j.compstruct.2021.114605.

[43] E. Etemadi, M. Gholikord, M. Zeeshan, H. Hu, Improved mechanical characteristics of new auxetic structures based on stretch-dominated-mechanism deformation under compressive and tensile loadings, Thin-Walled Struct. 184 (2023) 110491, https://doi.org/10.1016/j.tws.2022.110491.

[44] Y. Gao, Z. Zhou, H. Hu, J. Xiong, New concept of carbon fiber reinforced composite 3D auxetic lattice structures based on stretching-dominated cells, Mech. Mater. 152 (2021) 103661, https://doi.org/10.1016/j.mechmat.2020.103661.

[45] E. Etemadi, M. Zhang, K. Li, M. Bashtani, M.M. Po Ho, D. Tahir, H. Hu, Load-bearing characteristics of 3D auxetic structures made with carbon fiber reinforced polymer composite, Compos. Struct. 319 (2023) 117206, https://doi.org/10.1016/j.compstruct.2023.117206.

[46] W. Abd-Elaziem, S. Elkatatny, A.-E. Abd-Elaziem, M. Khedr, M.A. Abd El-baky, M.A. Hassan, M. Abu-Okail, M. Mohammed, A. Järvenpää, T. Allam, A. Hamada, On the current research progress of metallic materials fabricated by laser powder bed fusion process: a review, J. Mater. Res. Technol. 20 (2022) 681–707, https://doi.org/10.1016/j.jmrt.2022.07.085.

[47] J. Ding, S. Qu, L. Zhang, M.Y. Wang, X. Song, Geometric deviation and compensation for thin-walled shell lattice structures fabricated by high precision laser powder bed fusion, Addit. Manuf. 58 (2022) 103061.

[48] P. Singh, V.K. Balla, A. Tofangchi, S.V. Atre, K.H. Kate, Printability studies of ti-6Al-4V by metal fused filament fabrication (MF3), Int. J. Refract. Met. Hard Mater. 91 (2020) 105249.

[49] M.Á. Caminero, A. Romero Gutiérrez, J.M. Chacón, E. García-Plaza, P.J. Núñez, Effects of fused filament fabrication parameters on the manufacturing of 316L stainless-steel components: geometric and mechanical properties, rapid prototyp, J. 28 (2022) 2004–2026.

[50] B. Dutta, F.H. (Sam) Froes, the additive Manufacturing (AM) of titanium alloys, Met. Powder Rep. 72 (2017) 96–106, https://doi.org/10.1016/j.mprp.2016.12.062.

[51] A. Nazir, O. Gokcekaya, K.M.M. Billah, O. Ertugrul, J. Jiang, J. Sun, S. Hussain, Multi-material additive manufacturing: a systematic review of design, properties, applications, challenges, and 3D printing of materials and cellular metamaterials, Mater. Des. 111661 (2023).

[52] P. Wang, J. Song, M.L.S. Nai, J. Wei, Experimental analysis of additively manufactured component and design guidelines for lightweight structures: a case study using electron beam melting, Addit. Manuf. 33 (2020) 101088, https://doi.org/10.1016/j.addma.2020.101088.

[53] B. Vayssette, N. Saintier, C. Brugger, M. Elmay, E. Pessard, Surface roughness of ti-6Al-4V parts obtained by SLM and EBM: effect on the high cycle fatigue life, Procedia Eng. 213 (2018) 89–97.

[54] I. Koutiri, E. Pessard, P. Peyre, O. Amlou, T. De Terris, Influence of SLM process parameters on the surface finish, porosity rate and fatigue behavior of as-built inconel 625 parts, J. Mater. Process. Technol. 255 (2018) 536–546.

[55] J.-R. Lee, M.-S. Lee, S.M. Yeon, D. Kang, T.-S. Jun, Influence of heat treatment and loading direction on compressive deformation behaviour of Ti–6Al–4V ELI fabricated by powder bed fusion additive manufacturing, Mater. Sci. Eng. A 831 (2022) 142258, https://doi.org/10.1016/j.msea.2021.142258.

[56] O. Cansizoglu, O.L.A. Harrysson, D. Cormier, H. West, T. Mahale, Properties of Ti–6Al–4V non-stochastic lattice structures fabricated via electron beam melting, Mater. Sci. Eng. A 492 (2008) 468–474, https://doi.org/10.1016/j.msea.2008.04.002.

[57] L. Xiao, W. Song, M. Hu, P. Li, Compressive properties and micro-structural characteristics of Ti–6Al–4V fabricated by electron beam melting and selective laser melting, Mater. Sci. Eng. A 764 (2019) 138204, https://doi.org/10.1016/j.msea.2019.138204.

[58] A. Du Plessis, S.M.J. Razavi, F. Berto, The effects of microporosity in struts of gyroid lattice structures produced by laser powder bed fusion, Mater. Des. 194 (2020) 108899, https://doi.org/10.1016/j.matdes.2020.108899.

[59] A. Ataee, Y. Li, D. Fraser, G. Song, C. Wen, Anisotropic Ti-6Al-4V gyroid scaffolds manufactured by electron beam melting (EBM) for bone implant applications, Mater. Des. 137 (2018) 345–354, https://doi.org/10.1016/j.matdes.2017.10.040.

[60] A. Cutolo, B. Engelen, W. Desmet, B. Van Hooreweder, Mechanical properties of diamond lattice Ti–6Al–4V structures produced by laser powder bed fusion: on the effect of the load direction, J. Mech. Behav. Biomed. Mater. 104 (2020) 103656.

[61] P. Li, Y.E. Ma, W. Sun, X. Qian, W. Zhang, Z. Wang, Fracture and failure behavior of additive manufactured Ti6Al4V lattice structures under compressive load, Eng. Fract. Mech. 244 (2021) 107537, https://doi.org/10.1016/j.engfracmech.2021.107537.

[62] S.Y. Choy, C.-N. Sun, K.F. Leong, J. Wei, Compressive properties of Ti-6Al-4V lattice structures fabricated by selective laser melting: design, orientation and density, Addit. Manuf. 16 (2017) 213–224, https://doi.org/10.1016/j.addma.2017.06.01.

[63] G. Del Guercio, M. Galati, A. Saboori, Innovative approach to evaluate the mechanical performance of Ti–6Al–4V lattice structures produced by electron beam melting process, Met. Mater. Int. 27 (2021) 55–67, https://doi.org/10.1007/s12540-020-00745-2.

[64] D. Wang, D. Zhao, X. Liang, X. Li, F. Lin, Multiple stages of smoking phenomenon in electron beam powder bed fusion process, Addit. Manuf. 66 (2023) 103434.

[65] O.L. Harrysson, O. Cansizoglu, D.J. Marcellin-Little, D.R. Cormier, H.A. West II, Direct metal fabrication of titanium implants with tailored materials and mechanical properties using electron beam melting technology, Mater. Sci. Eng. C 28 (2008) 366–373.

[66] Z. Eren, O. Gokcekaya, T. Nakano, Z. Mecitoğlu, In-plane quasi-static compression deformation of Ti6Al4V double arrow-headed lattice structures fabricated by electron beam powder bed fusion process: build orientation, scan speed and failure mechanism, J. Mater. Res. Technol. 27 (2023) 6192–6210, https://doi.org/10.1016/j.jmrt.2023.11.027.

[67] Damage evolution and element removal for ductile metals, Abaqus Anal. Users Guide (n.d.). http://130.149.89.49:2080/v6.13/books/usb/default.htm?startat=pt05ch24s02abm43.html (accessed October 14, 2022).

[68] S. Deb, A. Muraleedharan, R. Immanuel, S. Panigrahi, G. Racineux, S. Marya, Establishing flow stress behaviour of Ti-6Al-4V alloy and development of constitutive models using Johnson-cook method and artificial neural network for quasi-static and dynamic loading, Theor. Appl. Fract. Mech. 119 (2022) 103338, https://doi.org/10.1016/j.tafmec.2022.103338.

[69] G. Chen, C. Ren, X. Yang, X. Jin, T. Guo, Finite element simulation of high-speed machining of titanium alloy (Ti–6Al–4V) based on ductile failure model, Int. J. Adv. Manuf. Technol. 56 (2011) 1027–1038, https://doi.org/10.1007/s00170-011-3233-6.

[70] T. Zhou, J. Wu, J. Che, Y. Wang, X. Wang, Dynamic shear characteristics of titanium alloy Ti-6Al-4V at large strain rates by the split hopkinson pressure bar test, Int. J. Impact Eng. 109 (2017) 167–177, https://doi.org/10.1016/j.ijimpeng.2017.06.007.

[71] Dassault Systems, Abaqus Theory Manual, Abaqus Theory Man. (2016). http://130.149.89.49:2080/v6.11/pdf_books/THEORY.pdf (accessed September 4, 2022).

[72] W. Zhang, M. Tong, N.M. Harrison, Scanning strategies effect on temperature, residual stress and deformation by multi-laser beam powder bed fusion manufacturing, Addit. Manuf. 36 (2020) 101507.

[73] X. Tan, Y. Kok, Y.J. Tan, M. Descoins, D. Mangelinck, S.B. Tor, K.F. Leong, C. K. Chua, Graded microstructure and mechanical properties of additive manufactured Ti–6Al–4V via electron beam melting, Acta Mater. 97 (2015) 1–16, https://doi.org/10.1016/j.actamat.2015.06.036.

[74] R.R. Kamath, P. Nandwana, Y. Ren, H. Choo, Solidification texture, variant selection, and phase fraction in a spot-melt electron-beam powder bed fusion

[75] processed Ti-6Al-4V, Addit. Manuf. 46 (2021) 102136, https://doi.org/10.1016/j.addma.2021.102136.

[75] Z. Eren, F. Usta, Z. Kazancı, H.S. Türkmen, Z. Mecitoğlu, Axial Crash and Crush Response of Novel Nested Tube Designs, in: 12th Int. Conf. Mech. Behav. Mater. ICM12 Karlsr. Ger., 2015. https://doi.org/10.13140/RG.2.1.2267.3124.

[76] M.F. Ashby, L.J. Gibson, Cellular solids structure and properties, Cambridge University Press, 1998.

[77] V. Deshpande, M. Ashby, N. Fleck, Foam topology: bending versus stretching dominated architectures, Acta Mater. 49 (2001) 1035–1040.

[78] J. Simpson, Z. Kazancı, Crushing investigation of crash boxes filled with honeycomb and re-entrant (auxetic) lattices, Thin-Walled Struct. 150 (2020) 106676.

[79] L.J. Gibson M.F. Ashby Cellular solids 1997 Cambridge University Press Cambridge 10.1017/CBO9781139878326.

[80] J. Noronha, J. Rogers, M. Leary, E. Kyriakou, S. Inverarity, R. Das, M. Brandt, M. Qian, Ti-6Al-4V hollow-strut lattices by laser powder bed fusion, Addit. Manuf. (2023) 103637.

[81] H. Zhong, T. Song, C. Li, R. Das, J. Gu, M. Qian, The Gibson-Ashby model for additively manufactured metal lattice materials: its theoretical basis, limitations and new insights from remedies, Curr. Opin. Solid State Mater. Sci. 27 (2023) 101081.

[82] T. Han, D. Qi, J. Ma, C. Sun, Generative design and mechanical properties of the lattice structures for tensile and compressive loading conditions fabricated by selective laser melting, Mech. Mater. 188 (2024) 104840.

[83] Y. Tao, W. Li, K. Wei, S. Duan, W. Wen, L. Chen, Y. Pei, D. Fang, Mechanical properties and energy absorption of 3D printed square hierarchical honeycombs under in-plane axial compression, Compos. Part B Eng. 176 (2019) 107219, https://doi.org/10.1016/j.compositesb.2019.107219.

[84] G.W. Kooistra, V.S. Deshpande, H.N.G. Wadley, Compressive behavior of age hardenable tetrahedral lattice truss structures made from aluminium, Acta Mater. 52 (2004) 4229–4237, https://doi.org/10.1016/j.actamat.2004.05.039.

[85] I. Maskery, N.T. Aboulkhair, A.O. Aremu, C.J. Tuck, I.A. Ashcroft, Compressive failure modes and energy absorption in additively manufactured double gyroid lattices, Addit. Manuf. 16 (2017) 24–29, https://doi.org/10.1016/j.addma.2017.04.003.

[86] P. Li, Y.E. Ma, W. Sun, X. Qian, W. Zhang, Z. Wang, Mechanical behaviors and failure modes of additive manufactured Ti6Al4V lattice structures under compressive load, Thin-Walled Struct. 180 (2022) 109778, https://doi.org/10.1016/j.tws.2022.109778.

[87] S.Y. Choy, C.-N. Sun, W.J. Sin, K.F. Leong, P.-C. Su, J. Wei, P. Wang, Superior energy absorption of continuously graded microlattices by electron beam additive manufacturing, Virtual Phys. Prototyp. 16 (2021) 14–28, https://doi.org/10.1080/17452759.2020.1868656.

[88] Q. Sun, J. Sun, K. Guo, L. Wang, Compressive mechanical properties and energy absorption characteristics of SLM fabricated Ti6Al4V triply periodic minimal surface cellular structures, Mech. Mater. 166 (2022) 104241.

[89] P. Wang, F. Yang, G. Lu, Y. Bian, S. Zhang, B. Zheng, H. Fan, Anisotropic compression behaviors of bio-inspired modified body-centered cubic lattices validated by additive manufacturing, Compos. Part B Eng. 234 (2022) 109724, https://doi.org/10.1016/j.compositesb.2022.109724.

[90] T. Tancogne-Dejean, X. Li, M. Diamantopoulou, C. Roth, D. Mohr, High strain rate response of additively-manufactured plate-lattices: experiments and modeling, J. Dyn. Behav. Mater. 5 (2019) 361–375.

[91] Z. Zeng, C. Wang, Y.Z. Lek, Y. Tian, S.Y. Kandukuri, P.J.D.S. Bartolo, K. Zhou, Influence of microstructure on stainless steel 316L lattice structures fabricated by electron beam and laser powder bed fusion, Mater. Sci. Eng. A 859 (2022) 144225, https://doi.org/10.1016/j.msea.2022.144225.

[92] I.P. Seetoh, X. Liu, K. Markandan, L. Zhen, C.Q. Lai, Strength and energy absorption characteristics of Ti6Al4V auxetic 3D anti-tetrachiral metamaterials, Mech. Mater. 156 (2021) 103811, https://doi.org/10.1016/j.mechmat.2021.103811.

[93] S.D. Papka, S. Kyriakides, Experiments and full-scale numerical simulations of in-plane crushing of a honeycomb, Acta Mater. 46 (1998) 2765–2776.

[94] B. Han, L.L. Yan, B. Yu, Q.C. Zhang, C.Q. Chen, T.J. Lu, Collapse mechanisms of metallic sandwich structures with aluminum foam-filled corrugated cores, J Mech Mater Struct 9 (2014) 397–425.

[95] S.O. Obadimu, K.I. Kourousis, Load-rate effects on the in-plane compressive behaviour of additively manufactured steel 316L honeycomb structures, Eng. Struct. 273 (2022) 115063, https://doi.org/10.1016/j.engstruct.2022.115063.

[96] L. Dong, V. Deshpande, H. Wadley, Mechanical response of Ti–6Al–4V octet-truss lattice structures, Int. J. Solids Struct. 60 (2015) 107–124.